# Astronomical calibration of the Ocean Anoxic Event 1b and its implications for the cause of mid-Cretaceous events: a multiproxy record

**J. M. F. Ramos[1,2], J. F. Savian[1,3], D. R. Franco[4], M. F. Figueiredo[5], F. Frontalini[6], R. Coccioni[7], C. G. Leandro[1,4], M. Giorgioni[8], P. H. P. C. Vidal[8], G. Fazio[4,8], L. Jovane[9], N. Sabatino[10], R. I. F. Trindade[11], L. R. Tedeschi[12]**

[1] Programa de Pós-Graduação em Geociências, Universidade Federal do Rio Grande do Sul, Porto Alegre, Brazil.
[2] Petrobras, Exploration - Basin Analysis, Rio de Janeiro, Brazil.
[3] Instituto de Geociências, Universidade Federal do Rio Grande do Sul, Porto Alegre, Brazil.
[4] Coordenação de Geofísica, Observatório Nacional, Rio de Janeiro, Brazil.
[5] Petrobras, Research Center (CENPES), Rio de Janeiro, Brazil.
[6] Dipartimento di Scienze Pure e Applicate (DiSPeA), Università degli Studi di Urbino "Carlo Bo", Urbino, Italy.
[7] Università degli Studi di Urbino "Carlo Bo", Urbino, Italy.
[8] Universidade de Brasília, Instituto de Geociências, Programa de Pós-graduação em Geologia
[9] Instituto Oceanográfico, Universidade de São Paulo, São Paulo, Brazil.
[10] Istituto per lo studio degli Impatti Antropici e Sostenibilità in ambiente marino (IAS-CNR), Palermo, Italy
[11] Instituto de Astronomia, Geofísica e Ciências Atmosféricas, Universidade de São Paulo, São Paulo, Brasil.
[12] Petrobras, LIBRA, Rio de Janeiro, Brazil.

Corresponding author: João M. F. Ramos (j.m.f.ramos@petrobras.com.br)

**Key Points:**

- 405-kyr cycles in the magnetic suscepbility and XRF data indicate an astronomically paced deposition at PLG core during OAE 1b.
- High-resolution chronostratigraphic study provides a timespan of 2.68 Myr for the Oceanic Anoxic Event 1b.
- OAE 1b results from the combination of warm climate, heavy precipitation and intense weathering, acting as amplifiers of orbital forcings.

## Abstract

Cyclostratigraphic analyses were performed on magnetic susceptibility (MS), and elemental Ti and Fe series along the upper Aptian-lower Albian interval of the Poggio le Guaine (PLG) core, a Cretaceous pelagic succession in the Umbria-Marche Basin (central Italy). This interval represents one the most detailed and complete sedimentary archives and records oceanic perturbations associated with Oceanic Anoxic Event (OAE) 1b. The MS, Ti and Fe orbital control indicates a timespan of 2.68 Myr for OAE 1b event (114.10 to 111.34 Ma) and short eccentricity cycles played a key role, in controlling the amount of detrital input from weathering during monsoonal periods. Our chronostratigraphic study also provides age of 114.09 Ma for 113/Jacob, 113.25 Ma for Kilian, 112.67 Ma as a central age of the Monte Nerone cluster, 111.70 Ma for Urbino and 111.37 Ma for Leenhardt subevents, and a timespan of ~20 kyr for 113/Jacob, 70 kyr for Kilian, 670 kyr for Monte Nerone cluster, 60 kyr for Urbino and 60 kyr for Leenhardt levels. This study provides compelling evidence of the enormous potential C-isotope stratigraphy as tie points for cyclostratigraphic studies and as a valuable way to evaluate diachronism of bioevents. The organic-rich levels encompassing OAE 1b event has particular characteristics resulting from the combination of warm climate triggered by volcanic $CO_2$ input, heavy precipitation, intense weathering and rapid marine transgressions, which leads the oceanic-atmospheric perturbations, acting as amplifiers of orbital forcings paleoclimate changes, resulting in deoxygenation and carbon burial during OAE 1b.



## Plain Language Summary

The cause and effect of the Cretaceous Oceanic Anoxic Events (OAEs) are a motive of debate in the literature. One of the most important limitations to answer these questions is the age and duration of these events. The age uncertainty makes the correlations unreliable because the cause-effect is necessary to be time-dependent. In this work, we show the age and duration of the OAE 1b in different records and provide a correlation with orbital forcing and volcanic activity.

## 1 Introduction

The Cretaceous greenhouse climate system was punctuated by the occurrence of Oceanic Anoxic Events (OAEs) of regional to global expression (Schlanger & Jenkyns, 1976; Leckie et al., 2002; Herrle et al., 2004; Jenkyns, 2010), commonly characterized by enhanced marine productivity and oxygen deficiency that led to a great accumulation of organic matter at the seafloor and the deposition of black shale layers (Jenkyns, 2010).

The OAE 1b is a ca. 3 Myr long-lasting event (Leckie et al., 2002; Trabucho Alexandre et al., 2011; Coccioni et al., 2014; Sabatino et al., 2015, 2018) characterized by the occurrence of multiple subevents as prominent black shale layers in the Umbria Marche and Vocontian basins, namely 113/Jacob, Kilian, Urbino/Paquier, and, Leenhardt levels or equivalent (e.g., Coccioni et al., 2014; Kennedy et al., 2014; Bottini et al., 2015; Sabatino et al., 2015; Kennedy et al., 2017; Bottini and Erba, 2018; Matsumoto et al., 2020; Bodin et al., 2023). These layers are related to short-duration events of increased marine primary productivity and preservation of organic matter (Bodin et al., 2023) of continental origin (Sabatino et al., 2015) with occasionally e substantial marine contributions (Sabatino et al., 2015; Bodin et al., 2023).

The OAE 1b has been associated to global climate warming, with average sea surface temperature (STT) between 34°C and 36°C, and high ocean primary productivity (McAnena et al., 2013; Bottini et al., 2015; Bottini & Erba, 2018; Browning & Watkins, 2008; Sabatino et al., 2015), superimposed on influx of continental organic matter (Wang et al., 2022; Bodin et al., 2023). Such high productivity conditions may have been triggered by the emplacements of large igneous provinces (LIPs) such as the Southern Kerguelen (SK), Nauru-Mariana Plateau (NMP) and Ontong Java Plateau (OJP) (Eldholm & Coffin, 2000; Matsumoto et al., 2021, 2022; Davidson et al., 2023), modifying the paleoclimate and terminating the Cold Snap period (McAnena et al., 2013). Micronutrients originating during the emplacement of the LIPs might have fertilized the surface ocean and stimulated the marine primary productivity before and during the OAE 1b (e.g., Leckie et al., 2002; Browning & Watkins, 2008).

Unlike OAE 1a, characterized by a single condensed section deposited over ~1 Myr (Leandro et al., 2022), OAE 1b can be understood as a protracted long-lasting interval of organic carbon burial (Sabatino et al., 2015), with a cluster of several and extreme short-duration subevents (Grippo et al., 2004; Huang et al., 2010; Sabatino et al., 2015; Charbonier et al., 2023; Ait-Itto et al., 2023) and represents the longest perturbation of the global carbon cycle during the

Cretaceous period (Sabatino et al., 2015). The difference between OAE 1a and OAE 1b is also visible in the Osmium isotope, a suitable proxy for tracing hydrothermal activity, reveals marked differences between these two events (i.e., OAE 1a and OAE 1b). The former is characterized by a significant $^{187}Os/^{188}Os_i$ shift, while the second exhibits only some subevents that can be associated with volcanism and others with a possible monsoonal origin for some levels of OAE 1b (Matsumoto et al., 2022).

In the 1980s, OAE 1b was not individualized with a specific event, being described as part of the "Aptian-Albian OAE" (Schlanger & Jenkyns, 1976). Arthur et al. (1990) distinguished the Aptian/Albian anoxic events into OAE 1a and OAE 1b, proposing subevents or short-term organic carbon burial episodes associated with marine transgressions. Herrle et al., (2004) constrained OAE 1b in the Aptian-Albian boundary, a section considerably restricted when compared to the definition by Coccioni et al. (2014) and the GTS2020. Some authors pointed out that Paquier Level is the sole representative of OAE 1b due to its exclusive 'paper-shale' characteristic and the heaviest $\varepsilon^{205}$ Tl anomaly as a proxy for globally significant ocean deoxygenation (Wang et al., 2022).

In this present work, the nomenclature used for OAE 1b follows Coccioni et al. (2014) for the Umbria-Marche Basin (UMB, central Italy) and Bodin et al. (2023) for the Vocontian Basin (France), where high concentrations of Hg (Sabatino et al., 2018), along with the continuously increasing trends of strontium and oxygen isotope not allow characterizing OAE 1b as a single event, but rather as a complex multiphase set of mostly negative $\delta^{13}C$ excursions spanning the Aptian/Albian interval containing widespread organic-rich layers. ).

The central–western Tethyan pelagic succession in the UMB holds complete and undisturbed records of the Aptian–Albian stages (Coccioni et al., 2012) including the lithological expression of the OAE 1b in the Marne a Fucoid Formation. The lithology of this formation consists of grayish-greenish, pelagic marls and marly limestones, alternating with black shales, but it is also characterized by some thick red-beds (e.g., Coccioni et al., 2012; Sabatino et al., 2015, 2018). These lithological alterations underline highly variable redox conditions at the bottom of the basin and suggest very unstable paleo-environmental and oceanographical conditions (Giorgioni et al., 2012, 2017). In this context, orbital perturbations were capable to change the palaeoceanographic regime by influencing the dispersal mechanism of the continental detrital input and nutrient supply (Tateo et al., 2000; Herrle et al., 2015; Wang et al., 2022).

Bodin et al. (2023) suggested that rhythmic changes in monsoonal activity, paced by Milankovitch cycles (long eccentricity), and their effect on the accumulation of organic matter in continental wetlands, explain the periodic shift in the global carbon isotope record throughout the OAE 1b interval.

Since the early 2000s, several studies have aimed to date the events that occurred during OAE 1b, detailing the aspect of "time," including both the time involved in the deposition of organic-rich levels and the time elapsed between these levels. Grippo et al. (2004) integrated earlier works with a time-series of photographic log of the Piobbico core (central Italy) and recognized a total of 29 long-eccentricity (405 kyr) cycles that resulted in an inferred duration of 11.8 ± 0.4 Myr of Albian. Huang et al. (2010), using high-resolution grayscale series of the pelagic Marne a Fucoidi again in the Piobbico core, covered the first third of OAE 1b and obtained a duration of 2.17 Myr between the Jacob and Kilian events, with a duration of 40 kyr and 120 kyr respectively.

Coccioni et al. (2014) estimated a timespan of 3.8 Myr for the entire OAE 1b (ages inferred after Grippo et al., 2004; Huang et al., 2010 and; Ogg and Hinnov, 2012). The latest Geologic Time Scale 2020 (Gale et al., 2020) documented a timespan of 1.3 Myr and 4.2 Myr between the Jacob to the Kilian and OAE 1b (Jacob to Leenhardt levels), respectively. Leandro et al. (2022) performed a cyclostratigraphic analysis based on high-resolution multiproxy ($\delta^{13}C$, $\delta^{18}O$, MS and ARM) dataset from the Poggio le Guaine (PLG) core and inferred a duration of 0.8 Myr between the Jacob and Kilian levels, with a duration of 30 kyr and 90 kyr, respectively. On the basis of magnetic susceptibility (MS) data and absolute dating from Selby et al. (2009), Charbonier et al. (2023) determined a duration of 25 kyr and 32 kyr for the Jacob and Kilian levels, respectively. Ait-Itto et al. (2023) using MS data of two sections of Col de Pré-Guittard (Vocontian Basin) determined a of 4.03 Myr for the interval encompassing the Jacob to Leenhardt levels. These results indicate that an ample duration between ~2.5 and 6 Myr of OAE 1b. However, a multiproxy characterization for this high-resolution interval associated with recent tie points from Herrle et al. (2015) and Bornemann et al. (2023)(after Selby et al., 2009), and the new biostratigraphic temporal calibration for the Aptian-Albian boundary by Leandro et al. (2022), suggest a duration of 3 Myr.

Significant efforts have been undertaken for correlating stable isotopes across different basins (Herrle et al., 2004; Coccioni et al., 2014; Bottini et al., 2015 Herrle et al., 2015; Fauth et

al., 2022; Bornemann et al., 2023). Herrle et al. (2004), correlated various basins across different depositional environments ranging from terrestrial to hemipelagic settings. Herrle et al. (2015) correlated the carbonate carbon isotope composite age-calibrated curve (Ogg & Hinnov, 2012) with the geochemical records of Axel Heiberg Island, Nunavut (Canada) and expanded the identification of subevents to the North Atlantic. Fauth et al. (2022), through integration with biostratigraphy (planktonic foraminiferal and calcareous nannofossil bioevents) and carbon isotopes, conducted an astronomical calibration of a marine succession in the South Atlantic. Bodin et al. (2023) stated that the carbon isotope fluctuations across the OAE 1b cluster are the result of global disturbances in the carbon cycle that involved both atmospheric and oceanic systems, enabling the use of these fluctuations as universal tie points and suitable for cyclostratigraphic investigations.

This multidisciplinary study includes MS data, XRF (X-ray Fluorescence) measurements, stable isotope $\delta^{13}C$ correlations. In this paper, we apply cyclostratigraphic methodologies to identify the signal of orbital cycles in interval encompassing the OAE 1b of the PLG core (Coccioni et al., 2012; Savian et al., 2016; Matsumoto et al., 2021, 2022; Leandro et al., 2022), with the aim of inferring the time, duration, sedimentation rates, and evaluating the climatic forcing along the record. Furthermore, we correlate the PLG section with the other available carbon isotopes curves (Herrle et al., 2004, 2015; Fauth et al., 2022; Leandro et al., 2022; Charbonier et al., 2023; Bornemann et al., 2023) and estimate the ages of the various organic-rich sedimentary rocks associated to OAE 1b. The aim of this paper is also to integrate the recent findings (carbon isotopic fluctuations, new absolute ages, new cyclostratigraphic orbital tests) and generate a new chronostratigraphic interpretation in this interval to enhance the understanding of temporal variations during the OAE 1b event.

## 2 Materials and Methods

### 2.1 Poggio le Guaine Records: section and core

The Cretaceous pelagic succession of the UMB was deposited in a complex geological setting along the continental margin of the Apulian block, which was moving along with Africa towards northern Europe at that time (Channell et al., 1979). After decades of research, the Aptian–Albian pelagic succession of the UMB has become a classic reference record for regional to global scale paleoenvironmental studies on OAEs (Coccioni et al., 2014; Sabatino et al., 2015;

Savian et al., 2016; ; Sabatino et al., 2018; Leandro et al., 2022; Matsumoto et al., 2020, 2021, 2022). This succession was deposited well above the calcite compensation depth (CCD) at middle to lower bathyal depths (1000-1500 m) and at a paleolatitude of approximately 20ºN, on the south western margin of the Tethyan Ocean (Arthur & Premoli Silva, 1982; Coccioni et al., 1987, 1989, 1990, 1992; Savian et al., 2016).

The Aptian-Albian pelagic succession of the UMB extends from the upper part of the Maiolica Fm. (Tithonian to lower Aptian) to the lower part of the Scaglia Bianca Fm. (upper Albian to lower Turonian) and includes the Marne a Fucoid Fm. in between. The upper part of the Maiolica Fm. is represented by centimeter thick beds of white to gray limestone interspersed with black shales. The lower part of the Scaglia Bianca Fm. is characterized by centimeter thick beds of yellowish-gray limestones with reddish limestones and an interval with centimeter thick black shale layers in the lower part (Pialli level, Coccioni, 2001), which is part of the sedimentary expression of the lower part of OAE 1d.

The PLG section outcrops in the eastern portion of Monte Nerone (Figure 1; latitude 43º32’29.06” N, longitude 12º34’51.09” E). Lithologies comprises pale reddish brown to dark reddish brown and pale olive to greyish olive argillaceous limestones and calcareous marlstones, marlstones, slightly calcareous mudstones to argillaceous mudstones with several cyclically alternating organic–rich black shales and mudstones (Coccioni et al., 2014).

The drilling site of PLG core is located 400 m northwest of the PLG section (Coccioni et al., 2012) and has a straightforward correlation with it (Coccioni et al., 2014) so that geochemical, isotopic and micropaleontological data of outcrop and borehole core can be confidently integrated (Matsumoto et al., 2020).

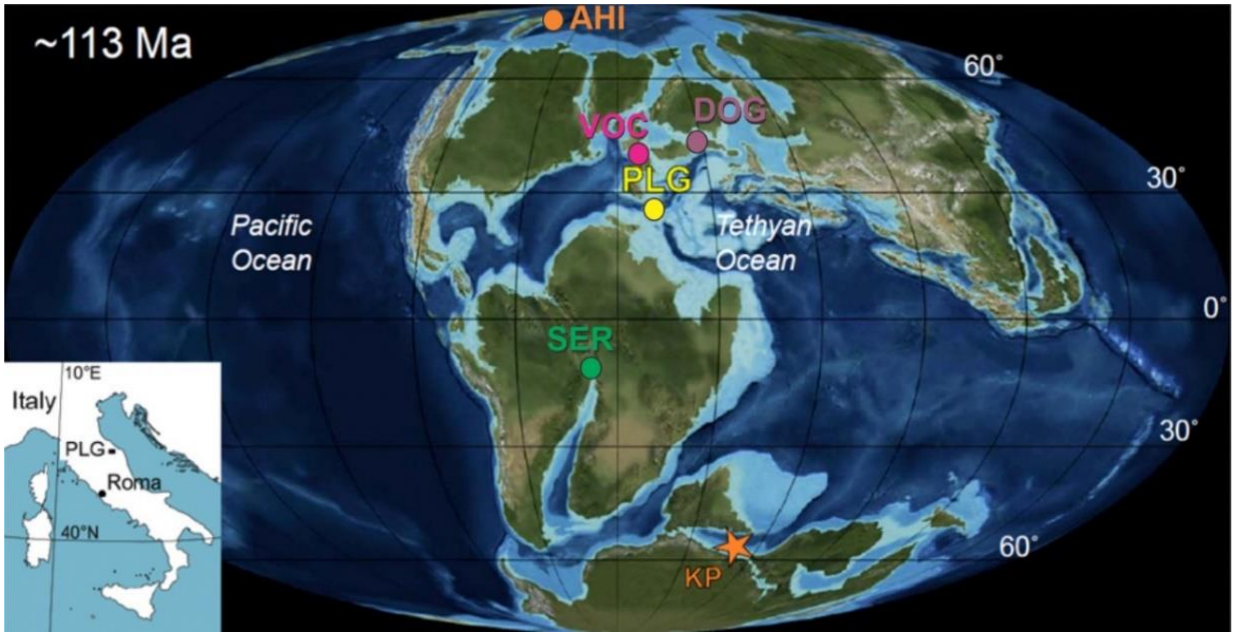


**Figure 1**. Paleogeographic reconstruction for the Aptian-Albian transition at ~113 Ma (modified after Sabatino et al., 2018) showing the location of the Poggio le Guaine (PLG), Vocontian Basin (VOC), Dolgen 3 core (DOG), Axel Heilberg Island (AHI), SER-03 core (SER) and of the Kerguelen Plateau (KP).

Several organic-rich horizons (Figure 2) representing the regional expression of the global OAE 1b have been identified (Coccioni et al., 1990, 2012; Coccioni, 1996; Leckie et al., 2002; Trabucho-Alexandre et al., 2011; Petrizzo et al., 2012; Coccioni et al., 2014; Sabatino et al., 2015, 2018; Matsumoto et al., 2020, 2022) and spanned from the upper Aptian to lower Albian (~114-109 Ma) (e.g., Coccioni et al., 2014). These events include the upper Aptian 113/Jacob, the lowermost Albian Kilian, the Albian Monte Nerone cluster, the Albian Urbino/Paquier, and the Albian Leenhardt levels (Coccioni et al., 2014; Sabatino et al., 2015, 2018; Matsumoto et al., 2020, 2022). According to the inferred ages of Leandro et al. (2022), the Aptian-Albian boundary is set at 113.0 Ma at PLG core in correspondence of the First Occurrence (FO) of *Microhedbergella renilaevis*, an age very similar to that attributed to Vöhrum's tuff (Selby et al., 2009).

High-resolution planktonic foraminiferal and calcareous nannofossil biostratigraphy, microfaunal (i.e., benthic and planktonic foraminifera, and radiolaria) assemblages, in combination with a detailed carbon and oxygen isotope record of the PLG section (Coccioni et al., 2014), associated with Os isotopic record (Matsumoto et al., 2020) and new preferred

plagioclase ages (Davidson et al., 2023) were used to characterize OAE 1b in this work (Figure 2).

This integrated stratigraphic framework was correlated with PLG core data to build the base of our study. The lithological description of PLG section presented in Figure 2 (Coccioni et al., 2014) was transposed to PLG core to better illustrate lithological differences. The "red" layers named as CORBs (*Cretaceous Oceanic Red Beds*) (Wang et al., 2009) appear related with new preferred plagioclase ages from OJP volcanism (Davidson et al., 2023) and show an intrinsic relationship with changes in the relative abundance of microfauna (Coccioni et al., 2014) reflecting regional paleoenvironmental conditions.

The GSSP of Aptian/Albian boundary (i.e. the base of the Albian Stage) has been defined at Col de Pré-Guittard (Vocontian Basin, southeast France) and corresponds to FO of the planktonic foraminifer *Microhedbergella miniglobularis* within the thin organic rich Niveau Kilian level (Kennedy et al., 2017; Gale et al., 2020) coinciding with a negative carbon isotope excursion. The drop in the abundance of planktic foraminifera relative to benthic species that globally occur in deep-sea records (Huber & Leckie, 2011) is also shown at the PLG section across the Aptian/Albian boundary (Coccioni et al., 2014).

The abrupt planktonic foraminiferal turnover across the Aptian–Albian boundary during OAE 1b can be ascribed to enhanced ocean acidification caused by the massive release of volcanic $CO_2$ (Matsumoto et al., 2020). Abrupt Os isotopic shift to unradiogenic values and elevated Hg concentrations suggest multiple submarine volcanic events that correlate with new plagioclase ages, further increasing the relationship between the OJP and the paleoenvironmental changes during OAE 1b (Sabatino et al., 2018; Matsumoto et al., 2020; Davidson et al., 2023). The absence of physical evidence of unconformable surfaces (Coccioni et al., 2014), the deposition above CCD (Coccioni, 1990), the presence of the M0r reversal Chron as main tie point for the Aptian base (Savian et al., 2016) make the PLG a suitable reference record, ideal to test cyclostratigraphic techniques and dating major geological events (e.g., isotopes excursions, bioevents, volcanic pulses). Also, the clear orbital forcing response of several Tethyan records (Tateo et al., 2000; Grippo et al., 2004; Huang et al., 2010; Leandro et al., 2022; Charbonier et al., 2023) have stimulated this new cyclostratigraphic evaluation.

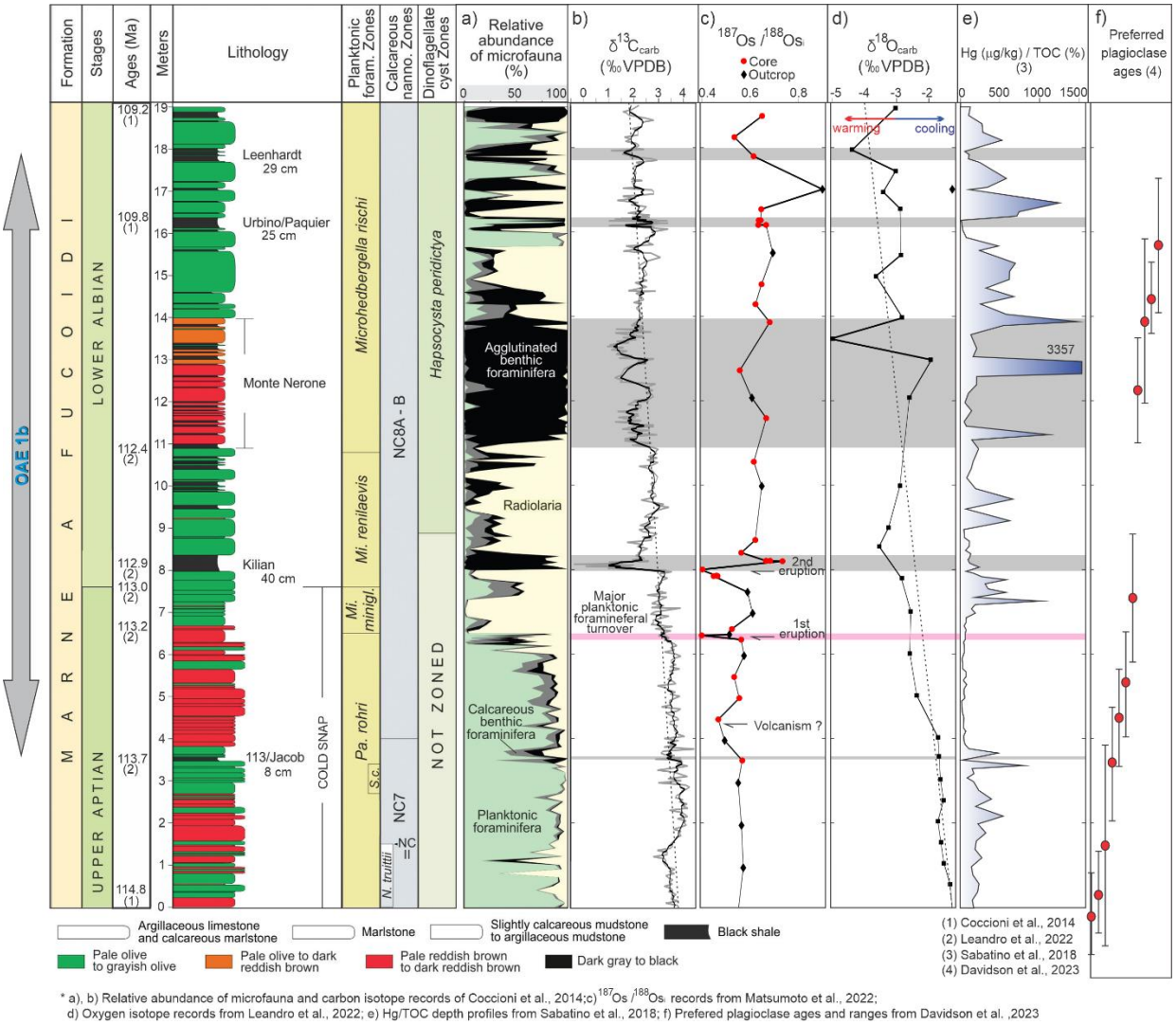


* a), b) Relative abundance of microfauna and carbon isotope records of Coccioni et al., 2014;c) $^{187}Os/^{188}Os$ records from Matsumoto et al., 2022;
d) Oxygen isotope records from Leandro et al., 2022; e) Hg/TOC depth profiles from Sabatino et al., 2018; f) Prefered plagioclase ages and ranges from Davidson et al. ,2023

**Figure 2.** Stratigraphy of Aptian-Albian transition at Poggio le Guaine plotted against (a) the relative abundance of microfauna from Coccioni et al. (2014); (b) $\delta^{13}C_{carb}$ data from Coccioni et al. (2014); (c) $^{187}Os/^{188}Os$ isotopic record from Matsumoto et al. (2020); (d), $\delta^{18}O_{carb}$ data from Leandro et al. (2022); (e) Hg/TOC depth profiles from Sabatino et al. (2018); (f) preferred plagioclase ages from Davidson et al. (2023). The diamond and asterisk mark highest occurrence of *Pseudoplanomalina cheniourensis* and the lowest occurrence of *Pleurostomella subnodosa*, respectively. Key to planktonic and calcareous nannofossil abbreviations: *Pa. = Paraticinella*, *Mi. = Microhedbergella*, *minigl. = miniglobularis*, *S. = Shackoina*, *c. = cepedai*, *N. = Nannoconus.*

296 2.2 Sampling

297 The PLG core was drilled in 2010 and designed to provide a high-resolution reference
298 record for the Aptian-Albian interval. Once in the laboratory, the core was split into two halves
299 along the dip line of the bedding. The left side (archived) of the core was plastic coated, packed
300 and housed at the University of Urbino (Italy). The right side (working half) of the core was cut
301 into four parts, comprising two lateral sections, a bottom section, and the center of the split core
302 (Savian et al., 2016). The center of the split core and bottom sections were cut in discrete cubic
303 samples from the center of the split core sections in cubes of ~8 $cm^3$ for environmental
304 magnetism analyses. Overall, we collected 3437 paleomagnetic samples with an averaging
305 spacing of ca. 3 cm, from 0 to 95 meters along the PLG core. The weight of each sample was
306 determined for subsequent mass normalization of magnetic properties. The same samples were
307 also used for isotopic analyses. For this study, we only focused on OAE 1b interval from 1 to 19
308 meters resulting in 639 paleomagnetic samples with an averaging spacing of ca. 2.8 cm. The
309 calcium carbonate ($CaCO_3$) content was compiled from Sabatino et al. (2015).
310
311 2.3 Magnetic susceptibility
312 The MS ($\chi$ mass specific normalized) measurements were carried out at the
313 Paleomagnetic Laboratory of the University of São Paulo (USPMag, Brazil). Frequency
314 dependence of the MS was measured in a total of 639 samples before remanence measurements.
315 Measurements of the MS were made on an MFK1-FA Multi-Function Kappabridge (Pokorný et
316 al., 2006) at three operating frequencies (976, 3904 and 15616 Hz) in a field of 200 A/m. For this
317 work, we only used the 976 Hz frequency for the cyclostratigraphic study.
318
319 2.4 XRF measurements
320 The XRF data were collected using a S1 Titan handheld XRF spectrometer, with a slit of
321 1 cm parallel and 0.7 cm perpendicular to the core length, and a sampling rate of 5 cm. Analyses
322 were made at the University of Urbino (Italy), conducted on the PLG core. A wide range of
323 chemical elements was identified with two tube voltage settings: at 10 kV and 50 kV, each with
324 five replicates and 30s acquisition time. After the measurement, anomalous values due to
325 alteration of the core surfaces or analytical issues were removed from the series and the data
326 were normalized respect to the total average of the series. Series of Ti and Fe were selected for

cyclostratigraphic analysis and for paleoenvironmental interpretations. Approximately 561 data points were measured to construct the XRF-derived elemental time Ti and Fe series.

### 2.5 Stable carbon and oxygen isotopes

Carbon ($\delta^{13}C$) and oxygen ($\delta^{18}O$) stable isotopes analyses were performed in the carbonate fraction were performed at the University of Oxford (UK). A total of 465 bulk-rock samples were collected every ~5 cm and used to characterize the OEA 1b event. A rotary drill was used to obtain powder from the cubes used for magnetostratigraphic measurements. During sampling, veins containing diagenetic carbonate were avoided. A total of six triplicates and 28 duplicates of the same depth were used to evaluate the reproducibility of the isotopic data. The powders of 313 samples were analyzed using a VG Isogas Prism II mass spectrometer with an online VG Isocarb common acid-bath preparation system at University of Oxford (UK). All these samples were cleaned using acetone [$(CH_3)2CO$] and dried at 60 °C for at least 30 min. The powders of 33 samples were analyzed using a Kiel IV carbonate device coupled to Thermo Delta V Advantage mass spectrometer and nine samples were analyzed using a Gas Bench II carbonate device coupled to a Thermo Scientific Delta V mass spectrometer. Samples were reacted with purified phosphoric acid ($H_3PO_4$) at 70–90°C in all instruments. The calibration was undertaken using the Oxford in-house Carrara marble standard (NOCZ) and NBS-19 (TS-Limestone). Data are reported relative to the Vienna Pee Dee Belemnite (VPDB) scale. The reproducibility of replicated standards (1σ) was < 0.09‰ for $\delta^{13}C$ and < 0.10‰ for $\delta^{18}O$. The maximum difference between triplicate and duplicate samples from the same depth were 0.31‰ for $\delta^{13}C$ and 0.39 ‰ for $\delta^{18}O$.

### 2.6 Cyclostratigraphic Analysis

Cyclostratigraphic analyses on MS and XRF-derived Ti and Fe records were realized by using *Acycle* software (Li et al., 2019) version 2.4.1. Regarding the MS dataset exhibited a non-stationary variance, it has been log-transformed for variance stabilization. Such pattern was not observed for the Fe and Ti datasets and hence it was not necessary to conduct the log-transformation. All series were then linearly interpolated every 2 cm, which is the mean spacing of the Fe, Ti and MS series. Prior to the spectral analysis, all datasets were detrended by using the “loess” method with a running window of 35% of the data lengths.

Spectral analysis was conducted by the prolate multitaper spectral estimator (MTM, Thomson, 1982) associated with the robust first-order autoregressive red-noise modeling (Mann & Lees, 1996). The persistence and/or transience of the astronomical signals along the series were assessed by means of Evolutive Harmonic Analysis (EHA) (Meyers et al., 2001). Regarding the best identification of the low-frequency spectral content at the MS-based analysis, we chose to solely discuss the results on the sediment average rate (SAR) (Meyers, 2015, 2019; Li et al., 2018) provided from the MS series. For this, we conducted a time-scale optimization analysis (*TimeOpt;* Meyers, 2015) in order to recover the optimal sedimentation rates and to evaluate the sedimentation accumulation rate (SAR) changes in MS data. Such results were further compared with the correlation coefficient (COCO) and evolutionary COCO (eCOCO) analyses (Li et al., 2018).

Potential astronomical frequencies that may correspond to those expected for the Tethyan pelagic succession in the UMB at Aptian–Albian times (Huang et al., 2010; Grippo et al., 2014; Leandro et al., 2022) were chosen based on the La2004 astronomical solution (Laskar et al., 2004). To convert MS and $\delta^{13}C_{arb}$ data from depth to time domain and, hence, to build an age model for the studied stratigraphic interval of the PLG core, we performed the astronomical tuning for MS series by means of a dynamically filtering (available at the *Acycle* package) that allows us to isolate the interpreted long-eccentricity component sinusoidal curve from the datasets tuned according to the La2004 $g_2$-$g_5$ target curve.

We used the $^{206}Pb/^{238}U$ absolute age of the basal Albian for the Schwicheldt Ton Member, Gault Formation, Vöhrum, Germany (Selby et al., 2009; Bornemann et al., 2023) and U-Pb age (111.74 ± 0.26 Ma, using bentonite zircons) dating of the Invincible Point Member of the Christopher Formation (Herrle et al., 2015) as tiepoints for astronomical tuning, and compare with the ages of Jacob and Kilian levels (Leandro et al., 2022). This tie point approach is quite different from previous cyclostratigraphic works for Aptian-Albian intervals as it overcomes the problem of diachronism between bioevents and enables correlation between basins.

## 3 Results

### 3.1 XRF

After normalization by mean and operation of dividing by the standard deviation, Ti normalized values vary from -2.4 to 5 and Fe from -2 to 3, and their variations could be used as

388 proxies of detrital supply (Herbert et al., 1986) and continental runoff (Arz et al., 1998). A more
389 distinct linear trend is observed in the Ti series compared to the Fe series; however, both datasets
390 exhibit a fairly similar pattern. It is possible to observe oscillations in the Ti and Fe profiles with
391 wavelengths of approximately 0.5 meters, modulated (superimposed) by cycles with 2 meters,
392 Figure 3. Cycles with great periods are also present, and some minima for these cycles coincide
393 with boundary of important intervals, like the Monte Nerone cluster (Figure 3b and 3c).
394 Prominent cycles with meter scale wavelengths (~0.5-0.7 m) coincide with the major planktonic
395 foraminiferal turnover and intervals with main paleoceanographic significance such as the Kilian
396 and Leenhardt levels, and some black shale levels in the Monte Nerone cluster (Figure 3b and
397 3c), suggesting that these features are somehow controlled by cyclical variations of this order of
398 magnitude.
399
400 3.2 Magnetic Susceptibility
401 The MS underlies the amount of magnetic minerals (e.g., Liu et al., 2020) and could also
402 be used as a proxy for detrital input throughout Fe minerals. Our MS record (mean of $\chi = 7.7 \times$
403 $10^{-8}$ $m^3/kg$) exhibited three stratigraphic long-term quasiperiodicies (~ 6 m) that would be partly
404 associated with microfaunal changes (Figure 3d). The 1.0-3.5 m basal interval is characterized
405 by the lowest values of MS that might be ascribed to low sedimentary input, which is followed
406 by a 5-m-thick interval marked by the highest values MS and reddish lithologies between
407 113/Jacob and below Kilian levels.
408 The Monte Nerone cluster (11.0 m – 14.0 m; Coccioni et al., 2014) is marked by
409 relatively stable MS values. Such lithostratigraphic interval is also characterized by a cyclic pair
410 of black shales and mudstones with the dominance of agglutinated foraminifera. The upper part
411 of the studied interval is quite different from the lower one. Short oscillations (~ 0.5 m
412 wavelengths) were noticed, which resemble a similar pattern observed at the microfaunal
413 variations and $CaCO_3$ content (Figure 3d and 3e). The Urbino/Paquier black shale (16.0 m – 16.4
414 m; Figure 3d) corresponds to a prominent negative short-term variation of MS.
415
416 3.3 $CaCO_3$ content
417 The percentages of $CaCO_3$, a proxy of surface carbonate productivity, ranges from 3 to
418 78 wt% (Figure 3e). The lowermost stratigraphic portion (1-11 m) exhibits a long-lasting

decreasing trend interrupted by short-term variations (from a few centimeters to a few meters) coinciding with intervals enriched in organic matter. Noteworthy, two coexisting bundling patterns (~ 0.5 m and ~ 1.0 m, respectively) are clearly observed, both displaying amplitude oscillations of approximately 20 wt%. Above the Monte Nerone cluster, the $CaCO_3$ values increase with respect to the lower interval. In general, low values of $CaCO_3$ are recorded in the black shale levels. A sharp decrease (from ~ 60 to ~30 wt%) was noticed at the same position of a foraminiferal turnover (Coccioni et al., 2014). Just above the OEA 1b onset, there is a three-meter interval (from 3.5 to 6.5 m) with higher $CaCO_3$ values (greater than 60 wt%.), which coincides to a higher MS value interval. Such interval, where apparently both MS and $CaCO_3$ contents evolve in phase (highlighted in blue, Figure 3e) is also coincident with the abnormally high Mn/Al ratio (Sabatino et al., 2015).

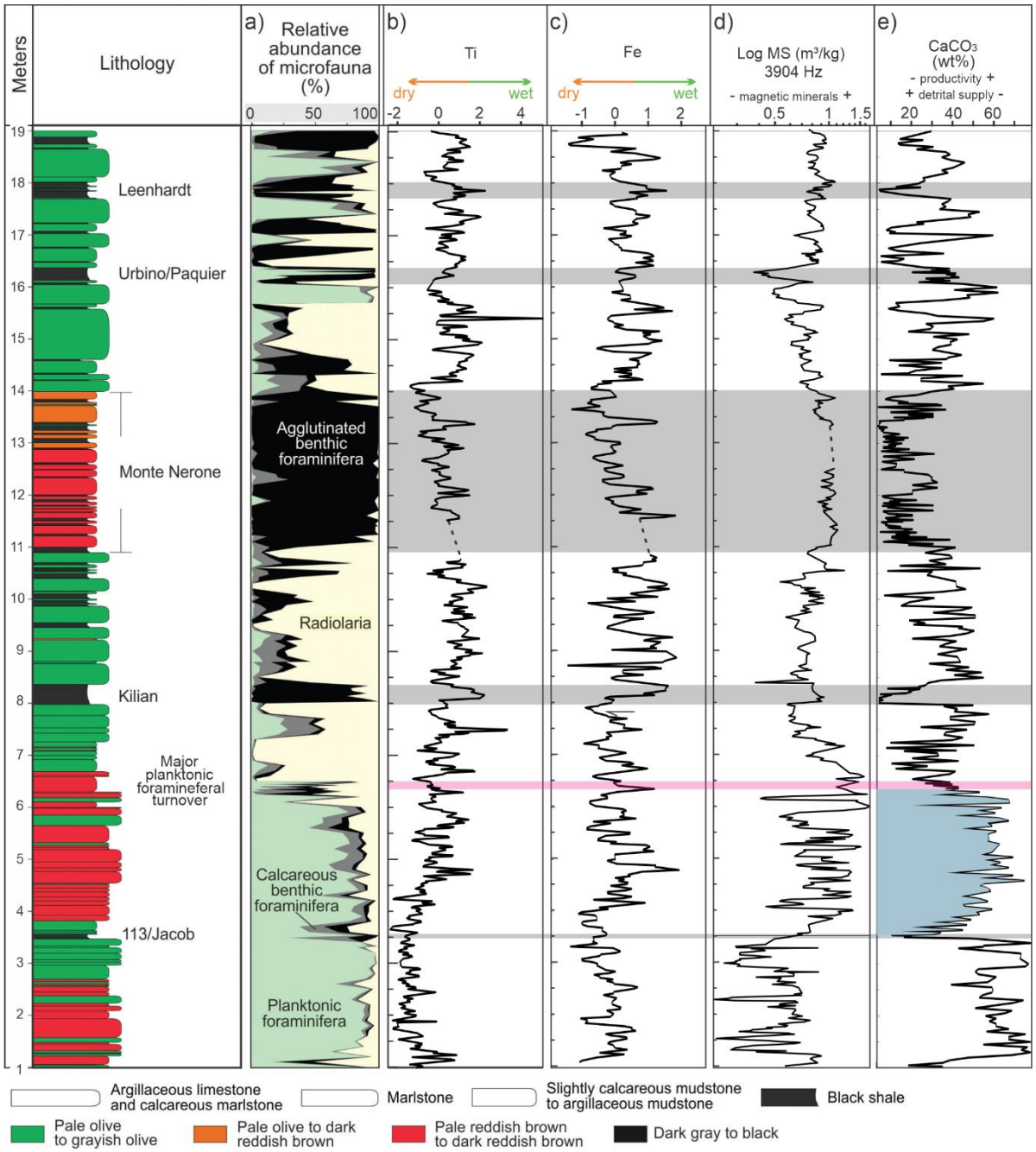


**Figure 3.** Lithology of the Poggio le Guaine section (Coccioni et al., 2014) plotted against the paleoclimatic proxies: (a) Foraminiferal and radiolarian abundance from Coccioni et al. (2014); (b) Ti content; (c) Fe content; (d) MS; (e) $CaCO_3$ from Coccioni et al. (2014). Pale blue represents a distinct interval where both MS and $CaCO_3$ present high values and are not in opposite phase.

### 3.4 Cyclostratigraphy

A number of studies (e.g., Huang et al., 2010; Grippo et al., 2014; Leandro et al., 2022) reported that Cretaceous sedimentary processes occurring along the pelagic Marne a Fucoidi Fm. in the UMB were controlled by orbitally induced climatic changes. In this work, the studied interval partially overlaps with the upper record of PLG core studied by Leandro et al. (2022), and we intend to verify whether the 405-kyr-based ATS inferred by this study could be extended upwards, hence reaching the OAE 1b interval.

Two long eccentricity cycles are expected between the Jacob and Kilian levels (comprising a timespan of ~ 810 kiloyears). Thus, the 405 kyr cycle should have an approximate wavelength of ~ 230 cm (~0.4 cycles/m). A spectral analysis was performed on the OAE 1b segment to identify the presence of these specific cycles and the others cycles at Milankovitch bands (Figure 4b and 4c). We compared the results obtained from various detrends before applying the LOESS detrend, elevating confidence levels of long and short eccentricity cycles. Despite the recognition of a visual record suggests the presence of a linear trend in the MS data, the comparison between the original spectrum harmonized by applying the logarithm and the same data after linear detrending (Figure supplementary S1) reveals that linear detrending before LOESS was unnecessary.

MTM-based spectral analyses of the Log MS datasets before and after detrending process (Figure 4d, e) exhibited a range of frequencies with significant spectral peaks exceeding the 90% confidence level (CL), with some peaks exceeding the 99% CL. After characterize values from 0.35 to 0.55 cycles/m as the spectral band of the long-eccentricity cycle (405 kyr) we could verify that low frequency spectral peaks (left portion of Figures 4e and 4f, highlighted by green bands) are associated with million-year scale band (MSB), and the two next peaks besides 405 kyr (right portion of Figures 4e,f, highlighted by blue bands) are associated with 125 kyr and 95 kyr short-eccentricity cycles, respectively, and the width of highlighted rectangles corresponding to Milankovitch period uncertainties (Waltham, 2015).

The same process could also be applied for estimating other cycles, predicted in the astronomical solution La2004 (Laskar et al., 2004), in Milankovitch band and defining the associated frequencies and wavelengths. Patterns revealed by combining the MTM and EHA analyses indicated that the spectral peaks (Log MS) with 243 cm, 71 cm and 55 cm could represent the expression of the 405-kyr, 125-kyr and 95-kyr eccentricity cycles (Figure 4e, f).

Other peaks ranging from 45-32 cm could be associated with secondary short eccentricity periods (Laskar, 2020). A careful analysis of LOESS trends reveals a combination of longer cycles (e.g., 1600, 1000 and 700 kyr) also suggesting a interesting link between MSB and CORBs intervals (red beds), not addressed in this study.

At the stratigraphic depth of ~ 13 m, there is a small interval (~ 40 cm) with a lack of magnetic susceptibility data (Figure 4), hindering the detection of cycles with wavelengths at the end of the short eccentricity. In order to test the feasibility of "interpolating" this interval, we conducted a comparison between Lomb-Scargle (Schulz and Stattegger, 1997) and MTM (Thomson, 1982) power spectra. The Lomb-Scargle power spectrum allows to perform the analysis of unevenly spaced time series, which are usually irregularly spaced in time and can be processed directly (Schulz and Stattegger, 1997). Despite the expected compromise in detecting high frequencies, the 405 kyr signal is present with the same characteristic band, enabling the continuation of the cyclostratigraphic analysis process (Figure S2).

The interpolation sampling rate could be a sensitive point of discussion. The XRF-derived series were acquired at 5 cm resolution rate, while the MS series at 2.8 cm. Since these rates exceed the interpolation performed in the cyclostratigraphic analyses (2 cm), it might raise questions, particularly when indicating the preservation of the precession signal along the PLG core. As we can see in Figure 5, the higher-frequency precession cycle has a wavelength of about 11 cm, and the overall resampling of all proxies to 2 cm does not impact the recognize of the Milankovitch cycles.

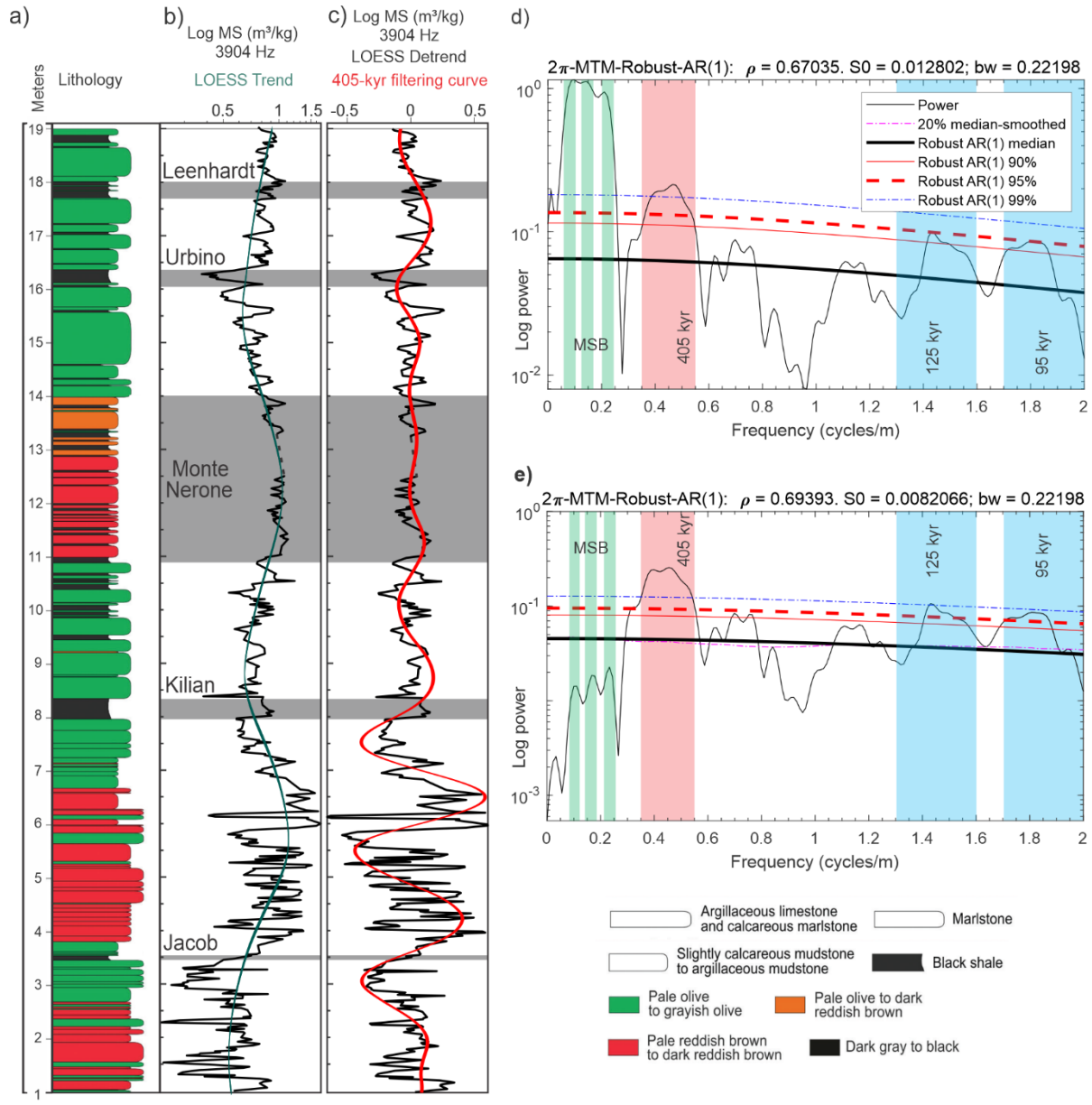


**Figure 4.** Detrend analysis for Log magnetic susceptibility (MS) depth-domain data for the PLG core: a) Lithology of the PLG section (Coccioni et al., 2014) transposed to PLG core. Grey bands represent the OAE 1b sub-events; b) Log MS (black line) record together with LOESS trend (green line) showing the inferred relationship between long-period cycles and CORBs intervals; c) LOESS detrend curve of Log MS data series (black line) together with 405 kyr filtered signal (red line); d) 2π MTM power spectrum associated with the first-order autoregressive (AR1) confidence levels showing the normal high power of Myr cycles compared to others cycles peaks. e) 2π MTM power spectrum associated with the first-order autoregressive (AR1) confidence levels after LOESS detrend. The colors at power spectrums are: pale green = MSB (million-year scale band); pale red = $E_{405}$; light blue = short eccentricity.

Comparing the power spectrum of MS (Figure 5a) with the predicted eccentricity and obliquity spectra (Figure 5c and 5d) in the astronomical solution by Laskar et al. (2004), it is possible to identify and correlate the major peaks within theoretical solutions. Assigning the median value of 0.44 cycles/m as the average frequency of the long-eccentricity cycle (wavelength 227.3 cm) we verified for specific spectral peaks in the Log MS ~ (227.3:71.4:52.6:21.3:14.9:12.8:10.9 = 20.7:6.5:4.8:1.9:1.4:1.2:1), resembling the predicted Milankovitch spectral peak ratios for Albian times (405:125:95:38.8:22.9:21.7:18.5=22:6.8:5.1:2.1:1.24:1.18:1) (Waltham, 2015) (Figure 5d).

The four eccentricity signals (cycles of 131, 125, 99, and 95 kyr), formed by the most powerful short eccentricity astronomical signals of La2004 (Laskar et al., 2004) and, simplified here as a pair composed of the e125 kyr ($g_4 - g_2$) and e95 kyr ($g_4 - g_5$) signals, are clearly visible next to the long eccentricity signal of 405 kyr. Additionally, we can observe the eccentricity peaks of e77 kyr ($g_2 + g_4 - 2g_5$) and e55 kyr ($g_3 + g_4 - g_2 - g_5$), although the former exhibits an excessively high-power value. The same outcome can be seen in Leandro et al. (2022), where the e77 kyr and e55 kyr frequency bands were described as transient periodicities. The frequency band of the e55 kyr signal (Figure 5b, light blue band), the short eccentricity signal with the highest frequency among the corresponding cycles (Laskar, 2020), appears to be nearly superimposed on the 51 kyr obliquity band ($p + s_6$), due the proximity of their frequencies. This proximity leads to a noteworthy increase in the power associated with the e55 kyr signal. In the La2004 solution, the obliquity signals related to the pair O39 kyr ($p + s_3$) and O37 kyr ($p + s_4$) exhibit the highest power when compared to the O51 kyr signal (Laskar, 2020). However, probably due to the simultaneous occurrence of this signal and the e55 kyr signal, there is an amplification in the power values. The pair of peaks related to the obliquity signals of O30 kyr and O29 kyr are also visible and correlational between the predicted and observed spectra (Figure 5a and 5c).

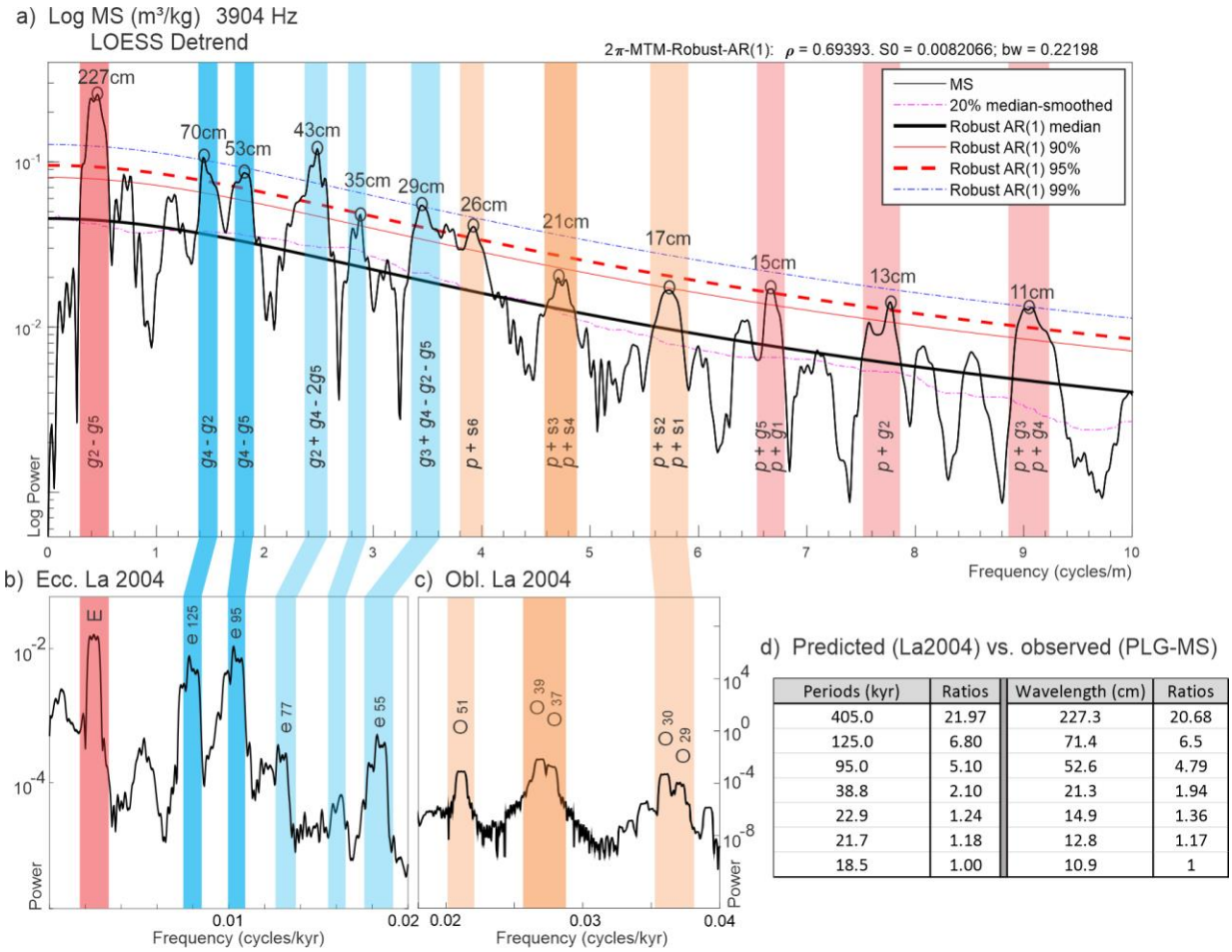


| Periods (kyr) | Ratios | Wavelength (cm) | Ratios |
|---|---|---|---|
| 405.0 | 21.97 | 227.3 | 20.68 |
| 125.0 | 6.80 | 71.4 | 6.5 |
| 95.0 | 5.10 | 52.6 | 4.79 |
| 38.8 | 2.10 | 21.3 | 1.94 |
| 22.9 | 1.24 | 14.9 | 1.36 |
| 21.7 | 1.18 | 12.8 | 1.17 |
| 18.5 | 1.00 | 10.9 | 1 |

**Figure 5.** Comparison between the power spectrum of magnetic susceptibility (MS) from the PLG core and the spectrum predicted in the astronomical solution La2004 (Laskar et al., 2004): a) Logarithmic MS displaying combinations of secular frequencies. The values of the respective cycle wavelengths (in centimeters) were extracted at the locations indicated by the black circles; b) La2004 astronomical solution (Eccentricity) for ages between 110 and 115 Ma; c) La2004 astronomical solution (Obliquity) for ages between 110 and 115 Ma; d) Comparison between the predicted (La2004) and observed (Log MS of PLG core) ratios for Albian times. The colors at power spectrums are: pale red = $E_{405}$; light blue = short eccentricity; Orange = Obliquity peaks (dark-orange, mean obliquity cycle); Pale Pink = Precession index peaks. More details about combinations of secular and fundamental frequencies described here are available at Laskar (2020).

After the analysis of MS data and the definition of the specific bands for each cycle, we performed a joint analysis of MS, Ti and Fe. LOESS detrend and MTM-based spectral analyses of the Ti, Fe and Log MS datasets exhibited a range of frequencies with significant spectral peaks exceeding the 95% CL (Figure 6a, 6b and 6c), with some peaks exceeding the 99% CL. The wavelength ratios verified for specific spectral peaks in the Ti ~

(217.4:66.7:55.6:20.4:14.3:12.2:10.9 = 20:6.13:5.1:1.9:1.3:1.12:1) and Fe ~ (219.8:66.7:55.6:22.7:15.1:13.9:10.9 = 20.2:6.13:5.1:2.1:1.4:1.05:1) spectra well correspond to the predicted Milankovitch spectral peak ratios for Albian times (405:125:95:38.8:22.9:21.7:18.5= 22:6.8:5.1:2.1:1.24:1.18:1) (Waltham, 2015). The combination of the MTM and EHA analyses suggested that the spectral peak bands with 260–210 cm, 70 cm and 60–54 cm wavelengths could be the expression of the 405-kyr, 125-kyr and 95-kyr eccentricity cycles, respectively. Other peaks ranging from 45-32 cm could be associated with secondary short eccentricity periods (Laskar, 2020).

Although we clearly identified an unequivocal record for the long and short-eccentricity cycles in Ti, Fe and MS data sets, it is also possible to recognize obliquity and precession cycles. The precessional cycle is present in the spectra with amplitudes near 99% CL revealing that the median sample rate of series is enough to preserve all Milankovitch cycles described in La2004 solution (Laskar et al., 2004).

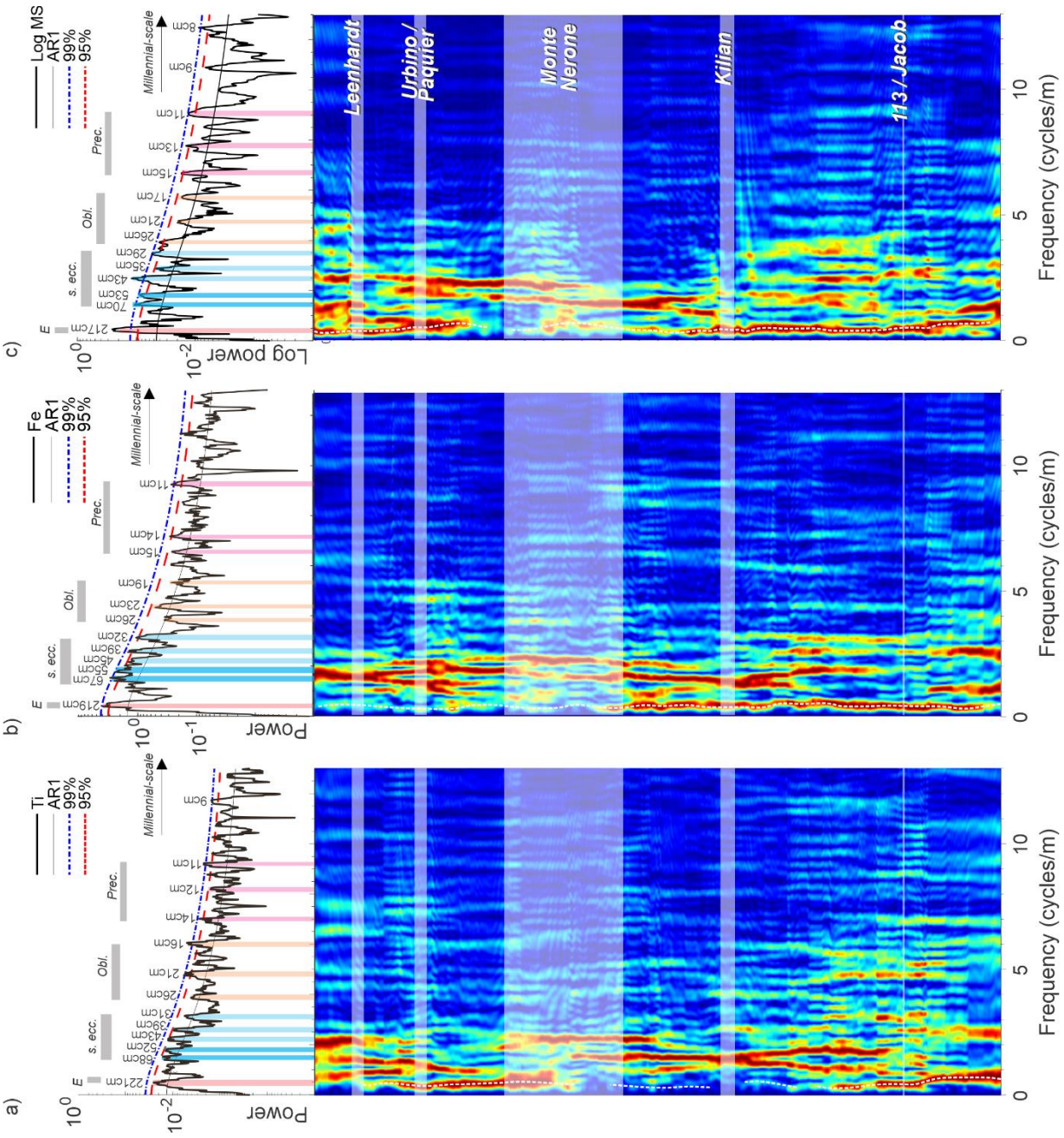


**Figure 6.** Cyclostratigraphic analyses for the LOESS detrended: a) Ti ; b) Fe and c) Log MS depth-domain data sets for PLG core. Top - 2π multi-taper method (MTM) power spectrum associated with the first-order autoregressive (AR1) confidence levels. Bottom - normalized amplitude of an evolutive harmonic analysis (EHA). The dashed line indicates the tracking wavelength record of the long-eccentricity ($E_{405}$) component for the datasets; d) The color bands in power spectrums represents $E_{405}$ – (pale red), short eccentricity (light blue); obliquity (orange), and precession index (light pink). White shaded areas represent major organic matter-rich levels of OAE 1b.

560 3.5 Phase relationship of Log MS data and Laskar's astronomical solutions

561 Before astronomical tuning process, we performed an evaluation of Log MS 405 kyr
562 filtered signal phase in relation to different Laskar's astronomical solutions (Laskar et al., 2004,
563 2011a, 2011b) (Figure 7). Vöhrum's tuff stratigraphic level is closely located above the carbon
564 isotope negative excursion of the Kilian level at Dolgen 3 core (Borneman et al., 2023) with an
565 age of 113.1 ± 0.3 Ma (Selby et al., 2009). The correlation between the 405 kyr signal extracted
566 from the MS curve and the approximate positioning of the tuff in relation to the Kilian level
567 indicates that the tuff is located near a peak (maximum) of long eccentricity. Based on the error
568 range of the absolute age from Selby et al. (2009), we can infer that the point of maximum
569 eccentricity in the cycle labeled with the letter "B" is the best candidate as a tie point.

570 Thus, 112.8 Ma is the minimal age (youngest) for the Vöhrum's tuff and the Kilian level
571 (little older) must be placed in the same long eccentricity cycle (Figure 7a). We do not know the
572 equivalent level of the Vöhrum's tuff in UMB, but carbon isotope correlations and the FO of
573 *Prediscosphaera columnata* constrain it within the *M. renilaevis* planktonic foraminiferal zone,
574 totally within a unique long eccentricity cycle (named here B, Figure 7a). As we can observe, the
575 age range related to the Vöhrum's tuff is likely in phase with the long eccentricity cycle named
576 'B,' and the negative excursion related to the Kilian Level in the $\delta^{13}C$ curve is located in the
577 decreasing portion of cycle 'B' towards the initial minimum of eccentricity in cycle 'A' (Figure
578 7c, yellow band). So, assuming the tuff's age is correct, it is unlikely that the negative excursion
579 of the Kilian level is correlatable with cycle 'A,' which has an approximate age of 113.6 Ma (as
580 suggested by Fauth et al., 2022).

581 Phases analysis of 405 kyr long eccentricity of Laskar's solutions indicate that between
582 113 and 113.2 Ma the maximum peaks of all Laskar's astronomical solutions are present and we
583 can associate the maximum of "B" Log MS filtered 405 cycles with any point in this interval
584 (Figure 7c). The maximum of "B" Log MS filtered 405 cycle (Figure 7a) is stratigraphically
585 above Kilian Level that is positioned at the PLG core in ascendent portion (between the
586 beginning of B cycle, or fist minimum, and the maximum of B) of the same cycle. So, it is
587 expected that the Kilian level must occur between 113.10 Ma (La2010b) – 113.24 (La2004) Ma.
588 It is worth mentioning that this age range does not invalidate or support other ages of Kilian
589 outside the Tethyan realm (Fauth et al., 2022; Leandro et al., 2022). The discussion of
590 synchronism of anoxic events around the world is not the objective of this work. We evaluated

two possibilities of phase relationship (direct=cave-cave and opposite=cave-peak) and concluded that, similar to Leandro et al. (2022), the direct way (cave-cave) is more plausible and double-check both tie points. High eccentricity values mean a high influx of terrigenous material and, consequently, higher Fe minerals concentration that increases MS values.

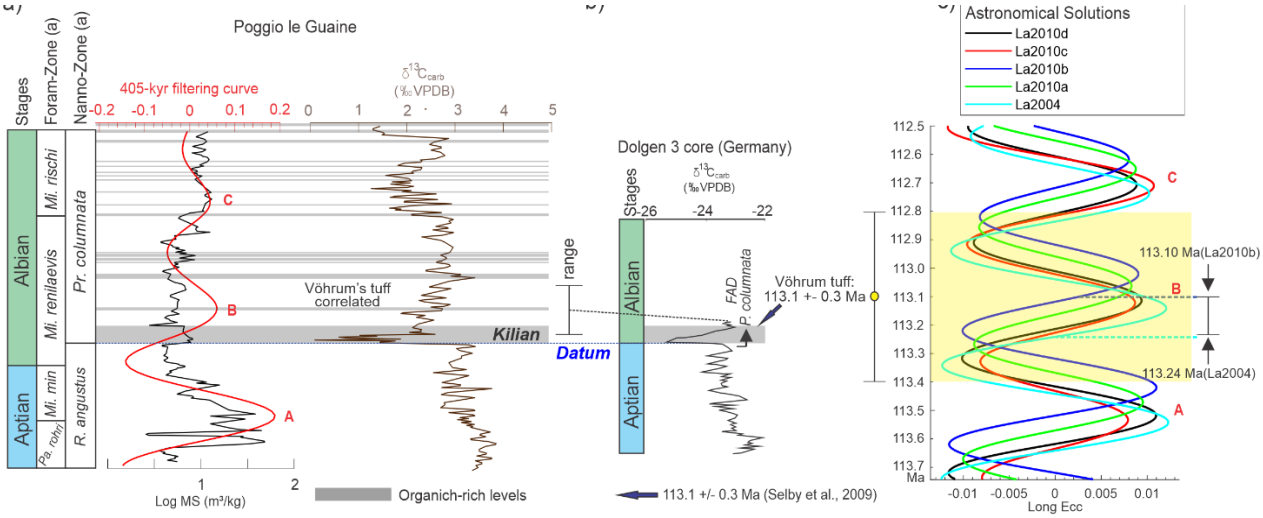


**Figure 7.** Evaluation of Log MS 405 kyr filtered signal phase of the Kilian Level based at different Laskar's astronomical solutions (Laskar et al., 2004, 2011a, 2011b): a) The Kilian Level at PLG core together with biozones (Coccioni et al., 2014) and 405 kyr Log MS filtered signal; b) Tentative of transpose Vöhrum's tuff stratigraphic position between Dolgen 3 core (Borneman et al., 2023) and PLG core; c) Phases of 405 kyr long eccentricity of Laskar's solutions indicate that age range of 113.0-133.2 Ma coinciding with the near maxima eccentricity of all solutions of a cycle named as B.

### 3.6 Tiepoints transposing process based on $\delta^{13}C$ chemostratigraphy

Since there are no available radiometric ages for the Aptian-Albian interval of the PLG core, it was necessary to transpose tiepoints between different places though correlations based on stable $\delta^{13}C$ chemostratigraphy. Even in distinct geological contexts (different depositional environments), the shapes of the $\delta^{13}C$ curves could be correlated to each other (Bodin et al., 2023) and use them as global tiepoints. These correlations aim to reconcile the $\delta^{13}C$ markers with numerical ages. We correlate carbon isotope stages (CIS) (Herrle et al., 2004; Coccioni et al., 2014; Leandro et al., 2022) and highlight prominent features, represented by excursions, peaks, troughs, and breaks in the long-term behavior of the carbon isotope curves, using the sequence of letters from the Greek alphabet, from ***α*** to **ο**, where: ***k*** is the onset of the Killian excursion and F.O. of *M. renilaevis*; **λ** is the Kilian prominent negative carbon excursion; **μ** is the end of this

614 excursion, coincident the Vöhrum tuff horizon (Bornemann et al., 2023), and the **o** marker
615 (positioned by correlation in ~17 m, at PLG) is stratigraphically placed very close to absolute U-
616 Pb 111.74 ± 0.26 Ma age estimation (bentonite zircons) from Herrle et al. (2015) (Table 1 and
617 Figure 8).

618 We also used stages definitions, foraminiferal and nannofossil events (Herrle et al., 2004,
619 2015; Coccioni et al., 2014; Leandro et al., 2022; Fauth et al., 2022; Bornemann et al., 2023) to
620 correlate CIS intervals, and match Glendonite beds (Herrle et al., 2015) as an effect of Cold Snap
621 interval to reinforce our age's transposition. The ammonite zones, even with the possibility of
622 occurrence in a limited region (Kennedy et al., 2014), have also been included in our
623 correlation's framework. We used transposed ages as anchors at the beginning of tuning process,
624 and later it was released during direct correlation between 405 kyr Log MS filtered signal.

625

626 **Table 1:** Major features associated with C-markers.

Table 1 Characteristics and positioning of c-markers into chemostratigraphic stages in PLG.

| C-marker | CIS | F.Z. | N.Z. | Characteristics |
|---|---|---|---|---|
| α | Ap 6-7 | *L. cabri* | NC 6 | Higher $\delta^{13}C$ peak at the base of a high values plateau in the *L. cabri* foraminiferal zone. |
| β | Ap 7 | *L. cabri* | NC 7 | Lower $\delta^{13}C$ peak within a high values plateau in the in *L. cabri* foraminiferal zone. |
| γ | Ap 7 | *G. ferr* | NC 7 | Higher $\delta^{13}C$ peak at end of a high values plateau in the *G. ferr.* foraminiferal zone. |
| δ | Ap 8 | *G. alger* | NC 7 | Lower $\delta^{13}C$ shift above a high values plateau at the base of the *G. alger.* foraminiferal zone. |
| ε | Ap 11-12 | *H. troc* | NC 7 | End of a low $\delta^{13}C$ values plateau and beggining o increasing trend in the *H. trocoidea* foraminiferal zone |
| ζ | Ap 12 | *H. troc* | NC 7 | End of a $\delta^{13}C$ increasing trend in the *H. trocoidea* foraminiferal zone |
| η | Ap 13 | *P.rohri* | NC 7 | Relatively higher $\delta^{13}C$ peak within a high values plateau across the *H. troc./Pa. rohri* foraminiferal zones. |
| θ | Ap 15 | *P.rohri* | NC 7 | Higher $\delta^{13}C$ peak at the top of a high values plateau in the *Pa. rohri* foraminiferal zone. |
| ι | Ap 15 - Al1 | *Mi.min* | NC 8A-B | Lower $\delta^{13}C$ peak at the top of a decreasing trend in the *Mi. min.* foraminiferal zone. |
| κ | Al1 | *Mi.ren* | NC 8A-B | Abrupt higher $\delta^{13}C$ peakin the *Mi. ren.* foraminiferal zone, preceding the Kilian negative excursion. |
| λ | Al1 | *Mi.ren* | NC 8A-B | Abrupt lower $\delta^{13}C$ peak in the *Mi. ren.* foraminiferal zone, associated with the Kilian event. |
| μ | Al1 | *Mi.ren* | NC 8A-B | Positive $\delta^{13}C$ shift in the *Mi. ren.* foraminiferal zone, above the Kilian negative peak. |
| υ | Al1 | *Mi.rischi* | NC 8A-B | Top of a $\delta^{13}C$ decreasing trend in the *Mi. rischi* foraminiferal zone. |
| ξ | Al 2-3 | *Mi.rischi* | NC 8A-B | Top of a $\delta^{13}C$ increasing trend in the *Mi. rischi / planispira* foraminiferal zone, near the Paquier event. |
| o | Al 3-4 | *Mi.rischi* | NC 8A-B | Abrupt break on $\delta^{13}C$ increasing trend in the *Mi. rischi / planispira* foraminiferal zone, Urbino event. |

627

628 The Aptian OAE 1a C-isotope excursion was explained by the emplacement of massive
629 OJP LIP (Bralower et al.,1999; Tedeschi et al., 2017). In the Tethys, the *Selli Level* (Coccioni et
630 al., 2014) and *Goguel Level* (Charbonier et al., 2023) or simply OAE 1a (Herrle et al., 2015,
631 Gale et al., 2020) events are black shales associated with this volcanism. However, new
632 $^{40}Ar/^{39}Ar$ data suggest that the eruptive history of the OJP was much younger (Davidson et al.,
633 2023), enabling an important link between the peaks of volcanism during OAE 1b (Matsumoto et
634 al., 2022) and OJP eruptions.

The top of OAE 1a event is characterized by a positive excursion name here by **α** (Figure 8) expressed as a higher $\delta^{13}C$ peak at the base of a high values plateau in the *L. cabri* foraminiferal zone. Positive long-term C-isotope trend is interrupted by a negative excursion (lower peak) detectable mainly in the Tethyan realm, associated with *Niveau Blanc* (Herrle et al., 2004; Charbonier et al., 2023) and *Wezel* (Matsumoto et al., 2020; Leandro et al., 2022), pointed as **β**. Leandro et al. (2022) dated this anoxic episode at 117.9 Ma. The upper part of the positive interval described as Ap 7 C-isotope stage (Herrle et al., 2004; Leandro et al., 2022) is followed by a huge negative excursion that coincides with *G. ferreolensis*/*G. algerianus* biostratigraphic zones boundary. The most $\delta^{13}C$ positive peak in *G. ferreolensis* at the end of high values plateau was named **γ**, a higher peak at end of a high values plateau.

The **δ** marker is clearly visible around all regions of Earth, associated with *NCC2* (Herrle et al., 2004; Charbonier et al., 2023) and *Noir* (Charbonier et al., 2023, Gale et al., 2020), also recognized by the long-term inflection change in the carbon isotope curve ,as a lower $\delta^{13}C$ shift above a high values plateau at the base of the *G. algerianus* foraminiferal zone. Except for the (relatively small) negative excursion associated with the Fallot level or FA 3, from this point onward, the curves show a gradual decrease in $\delta^{13}C$ values until the **ε** marker, where a significant shift in curve behavior occurs, and values begin to increase. These markers end a low $\delta^{13}C$ values plateau and begins an increasing trend in the *H. trocoidea* foraminiferal zone.

The **ε** marker is related to the onset of a C-isotope positive shift, which marks the beginning of a long interval with relatively high $\delta^{13}C$ values, in which the **ζ**, **η** and **θ** markers could be defined. This interval is related to a cooler period called *Cold Snap* in the Tethyan Ocean (McAnena et al., 2013; Bottini et al., 2015; Leandro et al., 2022; Bodin et al., 2023). The **ζ** marker is characterized as the end of a $\delta^{13}C$ increasing trend in the *H. trocoidea* foraminiferal zone, while the **η** marker is a relatively higher $\delta^{13}C$ peak within a high values plateau across the *H. trocoidea* / *Pa. rohri* foraminiferal zones.

Herrle et al. (2015) positioned the Jacob Level at Axel Heiberg below the position where the long-term trend of carbon isotope curve inflects, named as **η** marker. This feature is related to Ap 13 C-isotope stage in the Vocontian Basin, but Charbonier et al. (2023) dated the Jacob Level as a 114 Ma, within the Ap 15 C-isotope stage. Leandro et al. (2022) dated the Jacob event at 113.7 Ma that is characterized as a $\delta^{13}C$ negative excursion (Figure 8c).

The θ marker is the highest $\delta^{13}C$ peak at the top of a high values plateau in the *Pa. rohri* foraminiferal zone. Above this marker, the C-isotope curves slightly decrease and are punctuated by a short-term and high amplitude oscillation, marking the Kilian sub-event in the Tethyan realm (Bréhéret, 1983, 1988). The next interval is characterized by a decreasing trend representing Ap12-14, of which the lowest values are associated with the onset of OAE 1b event. Within the following decreasing trend, a rapid fluctuation occurs in the correspondence of the Kilian Level, a standout feature near the Aptian-Albian boundary (Herrle et al., 2004, 2015; Coccioni et al., 2014; Leandro et al., 2022; Fauth et al., 2022; Bornemann et al., 2023). The Kilian Level, labelled here as λ marker, is one of the most prominent features at the Aptian-Albian interval and an important marker for approximating the Aptian-Albian boundary (Petrizzo et al., 2012; Coccioni et al., 2014; Charbonier et al., 2023). It is characterized by a $\delta^{13}C$ positive excursion followed by a negative excursion in the Tethyan realm (Vocontian Basin and UMB).

The μ marker is a positive $\delta^{13}C$ shift in the *Mi. renilaevis* foraminiferal zone, above the Kilian negative peak. This level is associated with an age of 113 Ma (Gale et al., 2020; Leandro et al., 2022). The Vöhrum's tuff was identified above the Killian's excursion (Bornemann et al., 2023). The Kilian Level (top of Ap 15 C-stratigraphy stage or FO of *M. renilaevis*) shows a very minor positive excursion in the Atlantic Ocean (Axel Heiberg Island, North Atlantic Ocean and SER-0, South Atlantic Ocean) (Figure 8a and 8d). The Cedar Mountain Formation (USA) $\delta^{13}C$ curve also reveals a similar pattern (Ludvigson et al., 2010; Fauth et al., 2022).

Herrle et al. (2015) positioned the Kilian Level quite distant from the Albian base, with a U-Pb absolute age of 111.74 ± 0.26 Ma, using bentonite zircons for an interval remarkably close to the Kilian Level. In our correlation, this age corresponds to an interval close to ξ marker. Therefore, the signature that Herrle et al. (2015) attributed to the Kilian Level, is here correlated to the Paquier (ξ marker) or Urbino Level (Coccioni et al., 2015; Charbonier et al., 2023). Consequently, the interval attributed to the OAE 1b at Axel Heiberg Island (Herrle et al., 2015) is here related to the Leenhardt Level (Coccioni et al., 2015; Charbonier et al., 2023), and represented as a **o** marker.

The ξ marker represents a negative peak associated with the Paquier Level in the Vocontian Basin (Herrle et al., 2004), and a ~0.4‰ fluctuation corresponding to the Urbino

Level in the PLG record (Coccioni et al., 2014). Above, in the Al3-5 interval, the $\delta^{13}C$ curve reaches a minimum and then increases.

Below the **ν** marker, oscillations occur within the Monte Nerone interval at PLG without significant expressions in the isotopic curve in the Vocontian Basin, despite correlations between Monte Nerone and levels HN 3-HN 7 (Herrle et al., 2004; Coccioni et al., 2014). The Invincible Point Member of the Christopher Formation was dated at 111.74 Ma using bentonite zircons and falls close the **o** marker in the Axel Heilberg Island section (Herrle et al., 2015). The exact stratigraphic positioning of this dating is difficult to correlate with PLG and Vocontian sections, and thus, this was used solely as an age control point for the upper boundary of the studied section in the tuning process.

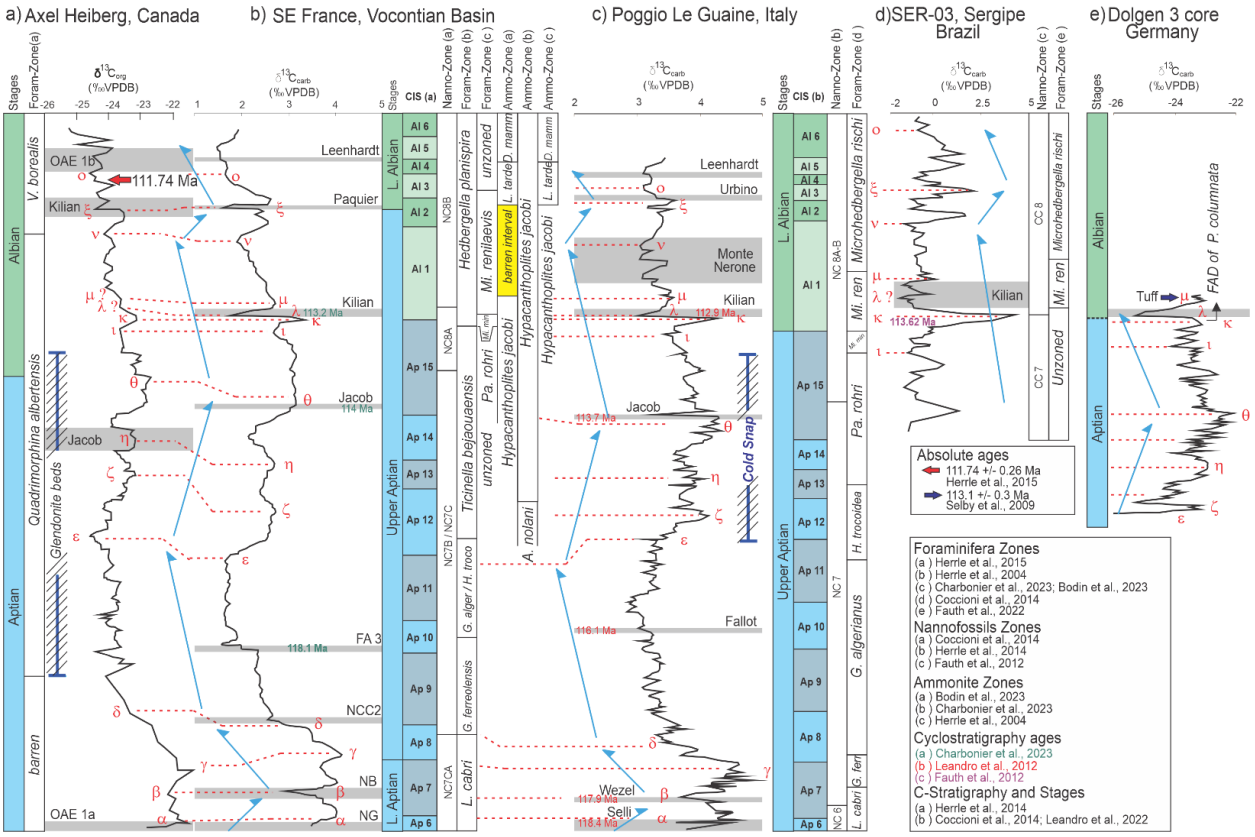


**Figure 8.** Correlation of C-isotope records showing the major patterns and C-marks of: a) Axel Heiberg Island, Canada; b) Vocontian Basin, France; c) PLG core, Italy; d) SER-03, Sergipe Basin, Brazil; e) Dolgen-3 core, Germany. Absolute ages and biozones are detailed in the legend. Grey shadings represent OAE 1b sub-events. Modified from Fauth et al. (2022), Leandro et al. (2022), Herrle et al. (2015),

711 Coccioni et al. (2014), Herrle et al. (2010), Boudin et al. (2023), Charbonier et al. (2023), Nebe (1999)
712 and Bornemann et al. (2023). Blue arrows indicate the long-term trends.
713
714 3.7 Astronomical tuning
715 Astronomical tuned Log MS data (Figure 9) were constructed after long-eccentricity
716 component interpretation in MS dataset with the La2004 astronomical solution (Laskar et al.,
717 2004). Figure 9a shows lithological changes along the PLG section (Coccioni et al., 2014)
718 alongside the cyclostratigraphically estimated ages determined in this study. Figure 9b provides
719 LOESS detrended Log MS dataset and 405 kyr dynamically filtered signal used for tuning,
720 anchored in CIS transposed absolute ages highlighted with red (111.74 ± 0.26 Ma, Herrle et al.,
721 2015) and blue arrows (113.1 ± 0.3 Ma, Selby et al., 2009) and the stratigraphic position of C-
722 isotope stages (Greek letters, in red). Using a dynamic filter with cut-off frequencies between
723 0.35 and 0.55 cycles/m, we isolated the interpreted 405-kyr long-eccentricity component within
724 the MS dataset. Then, we constructed the ~405-kyr tuned age model for the PLG utilizing the
725 output of this long-eccentricity filter (Figure 9b, red line) and aligning it with the $g_2$-$g_5$ target
726 curve from the La2004 astronomical solution (Figure 9d, red line) for the Aptian-Albian interval
727 (Laskar et al., 2004). This resulted in an average sedimentation rate of 0.5 cm/kyr (Figure 9c).
728 The sedimentation rate undergoes an increase from 0.42 to 0.65 cm/kyr until reaching the Monte
729 Nerone Level, after which it decreases to 0.47 cm/kyr, indicating a paleoenvironmental change
730 identifiable through a notable variation in sediment coloration.
731 This procedure allowed us to build a FATS based on a sequence of 9 long-eccentricity
732 cycles (E3 to E-5, written in red, where E0 is related to Kilian Level) and an age model for the
733 studied interval in the PLG core spanning ~3.4 Myr (19–1 m) (Figure 9e). For OAE 1b event
734 (i.e. from the base of Jacob Level to the top of Leenhardt Level) a timespan of ~2.76 Myr is
735 obtained. From the MS data age model, we can infer ages of ~113.55 Ma and ~113.33 for FO
736 and LO (last occurrence) *M. miniglobularis*, ~113.33 and ~112.82 Ma for FO and LO of *M.*
737 *renilaevis*, ~112.82, the latter coincides with FO *Microhedbergella rischi*. Also, we can infer
738 ages of major black shale levels in the PLG core. After tuning, we checked ages and timespan of
739 all geological features (e.g., biozones, black shales, CORBs) along the study interval and
740 estimated ages for C-marks. The ~1-m-thick bundles are associated with 405 kyr half-cycles,
741 while oscillations of around ~0.5 m exhibiting significant amplitudes are correlated with short

eccentricity cycles. These are modulated by longer cycles, contributing to a sedimentation rate ranging from ~0.4 to 0.8 cm/kyr. High frequency cycles (11-26 cm) created by obliquity and precession orbital modes are also present, where the latter is modulated by short eccentricity cycles.

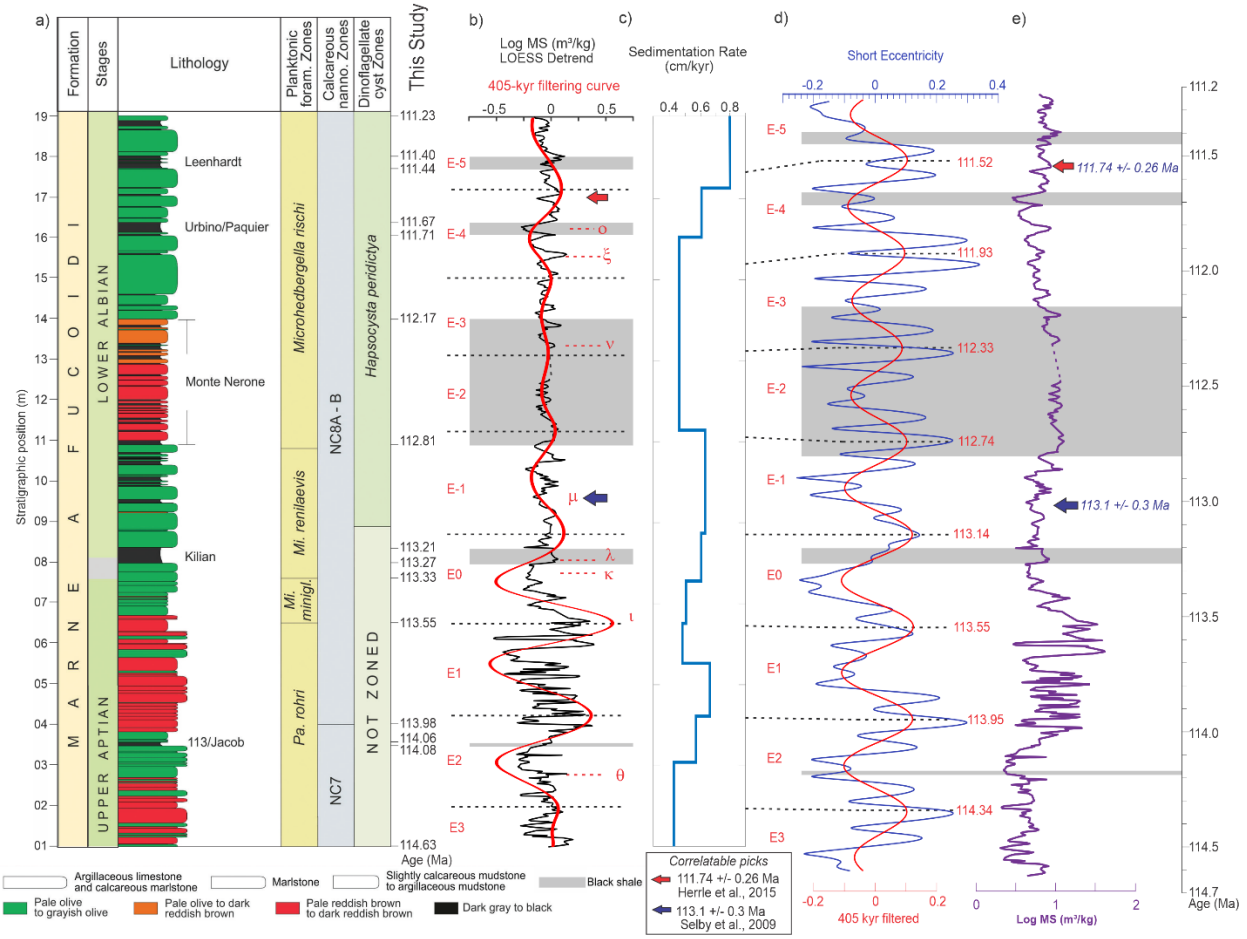


**Figure 9.** Astronomical calibration of the PLG core: a) Lithology, calcareous nannofossil and planktonic foraminiferal biostratigraphy from Coccioni et al. (2014), updated with new cyclostratigraphic ages on the right side; b) Log MS data and 405-kyr component filtered using dynamic filter, and (E) cycles denoted in red. The E-cycles and C-marks are presented in red letters and red and blue arrows represent transposed absolute ages used as tie points; c) The sediment accumulation rate (SAR) curve recovered on 405-kyr tuning (blue); d) La2004 orbital solutions (Laskar et al., 2004) for the eccentricity cycles of ~100 kyr (blue line) and ~405 kyr (red line); e) Astronomically tuned Log MS series (purple line). The major sub-events are highlighted in light grey.

758
759
760

761 3.8 SAR analysis

762 By integrating the existing biostratigraphy of the PLG section (Coccioni et al., 2014) with
763 the transposed absolute ages (Herrle et al., 2015; Bornemann et al., 2023) and the obtained ages
764 from our astronomical calibration, we were able to estimate a mean sedimentation rate of ~0.5
765 cm/kyr for the interval 1–19 m (Figure 10). This calculation was statistically tested by means of
766 *TimeOpt* analyses (Meyers, 2015). After LOESS detrend (Figure 10a and 10b), the Log MS
767 dataset is free from long cycles (up to 1 Myr), and values in the series become coherent with
768 modulation and correlations parameters in TimeOpt and COCO algorithms on Acycle.

769 The TimeOpt analysis over all LOESS detrended series (Figure 10a, b) indicates two
770 close possibles sedimentations rates (commonly referred to as SAR), and a $r^2$opt maximum at a
771 SAR of 0.55 cm/kyr (Figure 10e, red). The $r^2$ envelope regression model (Figure 10f, red)
772 suggests 0.41 cm/kyr as a SAR with maximum energy concentration, but a second large local
773 maximum occurs between 0.5 and 0.6 cm/kyr. The $r^2$ power (Figure 10f, grey) returns *p*-values
774 up 0.1 from 0.5-0.6 cm/kyr. The slight difference of ~0.15 cm/kyr between these SARs indicate
775 its suitability for cyclostratigraphic analyses (Weedon, 2003). The combination of $r^2$ envelope
776 and $r^2$ power ($r^2$ opt) estimates 0.55 cm/kyr as a best SAR (notable, an average SAR) for all
777 intervals.

778 Cross-plot of the data amplitude envelope and the TimeOp*t*-reconstructed eccentricity
779 (Figure 10g) indicate a SAR of 0.56 cm/kyr, punctuating that short-eccentricity cycles are
780 modulated by long-eccentricity, as shown in Figure 10h-j. Similar result was found using COCO
781 (Li et al., 2018), where correlation coefficient (Figure 10l) returns ρ-value up to 0.4 for SAR at
782 0.57 cm/kyr (ρ equal the Greek letter "rho"). The number of contributing astronomical
783 parameters (Figure 10m, dark blue) and the Null hypothesis (Figure 10m, red) crossing $10^{-2}$ $H_0$
784 significance level shows a good match at the same SAR reinforcing all previous observations.
785 For a detailed evaluation of SAR, we applied the evolutionary versions of COCO (named
786 eCOCO, Li et al., 2018).

787 eCOCO (Figure 10c) seems to better represent the SAR dependencies in tuning process
788 (Figure 10c, blue line), with SAR's variations following the results SAR of tuning. The

789 sedimentation rate at the base of the studied interval is 0.4 cm/kyr, which linearly increases to
790 higher value ~0.65 cm/kyr. This pattern follows the signal present in the series of Fe and Ti data
791 and may be associated with a change in the palaeoceanographic regime (i.e., combination of
792 increase in run-off, input of terrigenous material and enhanced weathering) after the Cold Snap
793 event (McAnena et al., 2013), when the warm and humid climate (typical of Cretaceous) was
794 established. The good match between SAR, eCOCO and Ti amount (Figure 10d) strongly
795 supports climate control, and specifically Ti amount suggests an increase in terrigenous input,
796 which controls the deposition. The monotonous (with slight variations) interval is interrupted by
797 a decrease of SAR (11-14m), related to the Monte Nerone mudstones and black shales. This
798 tendency of decreasing SAR value could be observed both eCOCO and tuning's SAR data, and
799 this regime persists upward. The Monte Nerone interval could be the result of another pulse of
800 cold waters paced by long periods cycles, as highlighted by LOESS trend (Figure 10b, dark
801 green line).

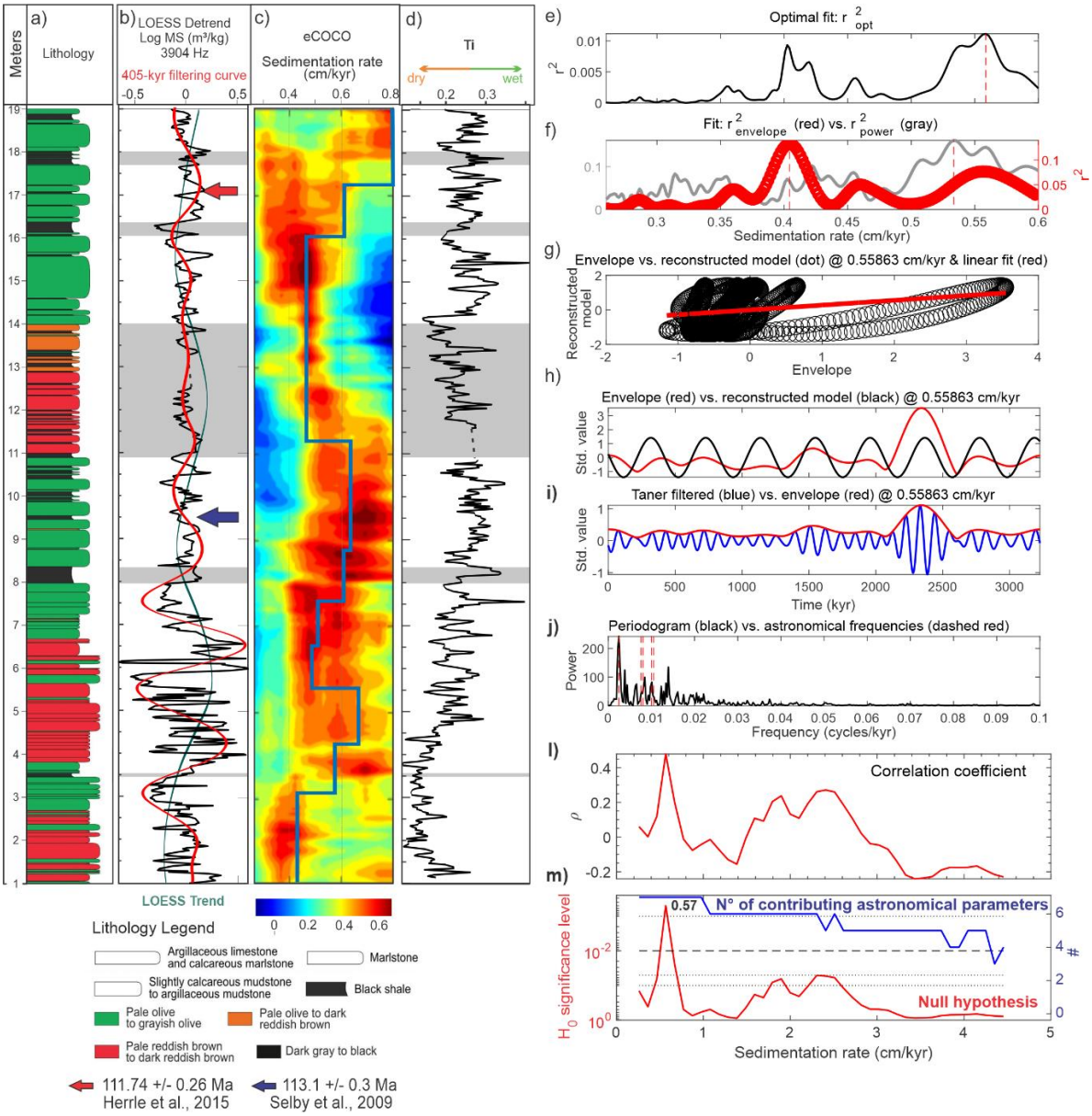


**Figure 10.** The sediment accumulation rates (SAR) analysis of the PLG core along the OAE 1b interval using TimeOpt, COCO and eCOCO methodologies: a) Lithology, described in Coccioni et al. (2014); b) LOESS trend (green line), 405 kyr signal (red line) of LOESS Log MS data (black line), presenting at least three long wavelengths cycles that were removed for the data series prior to the statistical analysis of SAR; c) eCOCO panel of LOESS detrend of Log MS data, plotted together with tuning process recovered SAR; d) Ti amount suggesting terrigenous input control of SAR; e-j) *TimeOpt* panels used for evaluating SAR in all intervals. It is notable secondary peaks due to regions within the studied interval where other rates of secondary sedimentation prevail. (l) COCO correlation coefficient with a great peak at 0.57 cm/kyr and value of $\rho > 0.4$. (m) The number of contributing astronomical parameters and the null hypothesis crossing $10^{-2}$ $H_0$ significance level also shows a good match with 0.57 cm/kyr SAR.

# 4 Discussion

## 4.1 Upper Aptian/lower-Albian floating astronomical timescale in the PLG core and C-isotope correlations

Our work provides a detailed upper Aptian-lower Albian time-depth framework for the PLG core. Through an astronomical calibrated age model, we are able to obtain the ages of OAE 1b sub-events and different zonal markers of calcareous nannofossils and correlated with planktonic foraminiferal zonal markers (Coccioni et al., 2012, 2014; Sabatino et al., 2015, 2018; Leandro et al., 2022). Previous studies have used a different age approach, which was based on duration of Albian Stage (Grippo et al., 2004; Huang et al., 2010). Leandro et al. (2022) used new M0r ages (Zhang et al., 2021) associated with high-precision U-Pb date of 113.1 ± 0.3 Ma (Selby et al., 2009) and provided a new age model for the Aptian with 405 kyr long-eccentricity cycle tuning based on the $g_2$-$g_5$ target curve from the La2004 solution for the Aptian–Albian.

On the other hand, using cyclostratigraphic techniques of SAR (Li et al., 2018; Meyers, 2015, 2019), we are able to estimate a sedimentation rate ranging from 0.4 to 0.6 cm/kyr for the interval 1–19 m. SAR slightly increases following the same trends of Ti and Fe contents, until the onset of the Monte Nerone black-shales cluster, where it drops below 0.5 cm/kyr and then it remains steady up to the Urbino Level. This result is consistent with the TimeOpt/COCO/eCOCO results (Figure 10).

As we used the same dataset of Leandro et al. (2022), we obtain similar SAR (mean of 0.43 cm/kyr) in the same intervals. The major difference is the tie point to anchor the 405 kyr long-eccentricity cycles, with a potential for generating a *bias* age effect. Vöhrum's tuff layer above carbon isotope negative excursion associated to the Kilian Level at Dolgen 3 core (Borneman et al., 2023) allows us to anchor the 405 kyr curve between 113.10 Ma (using the solution *La2010b* from Laskar et al., 2011b) and 113.24 Ma (using the solution *La2004*, from Laskar et al., 2004), as shown in Figure 7, providing greater precision to the tuning process since there is no longer a need to use the average value of 113.00 Ma as an anchor.

Table 2 shows estimated age for major OAE 1b sub-events. Previous studies have suggested a correlation between OAE 1a with the OJP basalt flows (Larson & Erba, 1999; Chambers et al., 2004; Tejada et al., 2009) and a rapid global warming, and elevated rates of silicate weathering both on the continents and in the oceans (Bottini et al., 2018).

844 However, new age constrains of the OJP show that the upper lava-flow units are much
845 younger (i.e., 115.51–111.42 Ma) than previously suggested (Davidson et al., 2023). These
846 numbers are consistent with our study, where the effect of enhanced weathering began near the
847 onset of the 113/Jacob Level, marked by increasing sedimentation rate and Ti and Fe contents
848 into the UMB. $^{187}Os/^{188}Os$ pulses related to the OAE 1b (Matsumoto et al., 2020) also support
849 this suggestion (Figure 2). The apparent diachronism between the onset of anoxic events in
850 different sections (e.g., Kilian at 112.9 Ma in Leandro et al., 2022 and 113.6 Ma in Fauth et al.,
851 2022) from different global regions may be attributed to age adjustments (anchor *bias*) and $\delta^{13}C$
852 correlation errors, as it can be observed in Figure 8.
853
854 **Table 2:** Comparison of ages of the organic-rich levels.
855

Table 2 Estimated ages of the black-shale levels.

| Work | Black-shale levels (estimated age in Ma) | | | | |
|---|---|---|---|---|---|
| | 113/Jacob | Killian | Monte Nerone | Urbino | Leenhardt |
| Huang et al., 2010 | 114.2 | 112 | | | |
| Coccioni et al., 2014 | 113.2 | 111.5 | | 109.8 | >109.2 |
| Sabatino et al., 2018 | 115.0 | 112.8 | | 111.3 | >110.7 |
| Leandro et al., 2022 | 113.7 | 112.9 | | | |
| Matsumoto et al.,2020 | 114.5 | 112.8 | | 111.1 | 110.5 |
| Fauth et al., 2022 | | 113.6 | | | |
| Charbonier et al., 2023 | 114.0 | 113.2 | | | |
| This work | $114.07^{114.06}_{114.08}$ | $113.24^{113.21}_{113.27}$ | $112.49^{112.17}_{112.81}$ | $111.69^{111.67}_{111.71}$ | $111.42^{111.40}_{111.44}$ |

856
857 After comparing the ages of OAE 1b sub-events, we must double-check their
858 stratigraphic position respect to the to our C-isotope markers (Figure 8). The 113/Jacob Level of
859 Huang et al. (2010) occurs near the base of the *Nannoconus regularis* calcareous nannoplankton
860 zone and within the *P. rohri* planktonic foraminiferal zone. Nonetheless, it is important to
861 mention that these two works used different tie points: Huang et al. (2010) used the Albian-
862 Cenomanian boundary at 99.6 Ma as a tie point for the tuning process, without using any
863 absolute radiometric age to anchor this boundary, while Charbonier et al. (2023) employed the
864 average age of the base of the Albian (113.2 ± 0.3 Ma by Gradstein et al., 2020, after U-Pb
865 dating of Selby et al., 2009) in the tuning process.
866 The high latitude Kilian Level of Herrle et al. (2015) corresponds to the benthic
867 *Verneuilinoides borealis* foraminiferal zone, and has a carbon isotope pattern that is quite
868 distinct from other patterns for the Kilian Level (Huang et al., 2010; Coccioni et al., 2014;

Kennedy et al., 2014; Kennedy et al., 2017; Leandro et al., 2022; Fauth et al., 2022; Bodin et al., 2023; Charbonier et al. 2023), represented here by the **λ** marker. In general, the Kilian Level is visible in C-isotope curves as a positive excursion followed by a negative, associated with *M. renilaevis* foraminiferal zone (Kennedy et al., 2014, 2017). The Vöhrum section and the ash layer at 113.1 ± 0.3 Ma (Selby et al., 2009) do not contain planktonic foraminifera, and the correlation between the two outcrops is based on ammonite associations (top of *Hypacanthoplites jacobi* ammonite zone) and the FO of *P. columnata* (subcircular category). *H. jacobi* ammonite zone extends into the early-Albian standard zonation of Ogg et al. (2016) and could be correlated not only with the Kilian Level (Bodin et al., 2023) but also with HK 3-6 key beds (Monte Nerone, in PLG) and the Paquier Level (Herrle et al., 2010). So, the Aptian-Albian boundary in the Vöhrum section (Selby et al., 2009), does not necessarily coincide with the Kilian Level and the age of 113.1±0.3 Ma could be the age of the Ap-15, Al-1 or Al-2 carbon isotope stages (Herrle et al., 2010).

Our astronomical tuning provides an age of 112.81 Ma for the base of the Monte Nerone interval (Coccioni et al., 2014) and of 111.71 Ma for the Urbino black shale level (**o** marker), remarkably close to the U-Pb 111.74 ± 0.26 Ma of the dated and extrapolated level of Herrle et al. (2015). For the **μ** marker, the Vöhrum tuff, we estimate an age of 113.0 Ma, which corroborates the 113.1 ± 0.3 Ma of the ash layer (Selby et al., 2009; Bornemann et al., 2023). Cyclostratigraphic analysis of Nebe (1999) estimated a median age of 113.25 Ma for the Kilian Level. The present work provides an age of 113.25 Ma for the **λ** mark (extreme point of negative excursion associated to the Kilian Level, PLG core) and 113.3 Ma for the **κ** mark (extreme point of positive excursion), corroborating the 113.2 Ma age of GTS2020 (Gale et al., 2020). If we used FO of *M. renilaevis* as marker for the Aptian-Albian boundary (e.g., Gradstein et al., 2020; Kennedy et al., 2014), we extrapolated an age of 113.33 Ma. However, to facilitate global correlations (oceans and continental sections) and avoid bioevents diachronism, we suggest adopting the **κ** carbon isotope as an alternative and visual marker of the Aptian-Albian boundary.

Our FATS matches well with absolute ages (Selby et al., 2009; Herrle et al. 2015; Bornemann et al., 2023) and carbon isotope stratigraphy of the PLG core and Vocontian Basin (Coccioni et al., 2014; Herrle et al. 2004). We have been able to define a time span of 2.76 Myr for the OAE 1b event meant, from the 113/Jacob to the Leenhardt levels (Matsumoto et al., 2020). For individual sub-events, we obtain the following ages 114.07 Ma for 113/Jacob, 113.25

Ma for Kilian, 112.49 Ma for the middle part of the Monte Nerone cluster, 111.69 Ma for Urbino and 111.42 Ma for Leenhardt levels (Table 2). The estimated timespan of the 113/Jacob black-shale is quite similar to previous studies (Table 3). As this study is the first to provide a timespan of the Monte Nerone, Urbino, and Leenhardt levels in the UMB, there is no other reference to compare our estimates. These results demonstrate that our FATS reasonably matches well with the timespan of similar cyclostratigraphic studies (Leandro et al., 2022; Charbonier et al., 2023).

**Table 3:** Comparison of timespan of Upper Aptian / Lower Albian the organic-rich levels.

Table 3 Estimated timespan of Upper Aptian / Lower Albian events.

| Work | Timespan (kyr) | | | | |
|---|---|---|---|---|---|
| | 113/Jacob | Killian | Monte Nerone | Urbino | Leenhardt |
| Huang et al., 2010 | ~40 | ~120 | | | |
| Coccioni et al., 2014 | | ~200 | | | |
| Leandro et al., 2022 | ~30 | ~90 | | | |
| Fauth et al., 2022 | | ~200 | | | |
| Charbonier et al., 2023 | ~25 | ~32 | | | |
| This work | ~20 | ~60 | ~640 | ~40 | ~40 |

4.2 C-isotope stages, their markers, and sub-events levels correlations in different basins

The PLG site, where the PLG core was drilled, provides one of the most continuous, complete, and best-preserved Aptian-Albian record and is represented by calcareous pelagic rocks extending from the Albian-Cenomanian boundary down to the uppermost Barremian (Coccioni et al., 2012). Several carbon-isotope excursions are observed in the $\delta^{13}C$ record of the PLG core (Coccioni et al., 2014; Leandro et al., 2022) and have a potential for long distance correlations.

In this work, we recognize significant landmarks (notable features separating the stages or within these stages), named here as C-markers, which have been observed in other records. We reviewed eight C-isotope stages around the OAE 1b interval, based on the correlation with other sections (Figure 11). This procedure allows us to transpose the ages of significant landmarks of carbon isotope ratios, and then attribute an age to each marker and C-isotope stage.

We obtained the following ages of C-isotope stages, in stratigraphic order: **θ** = ~114.2 Ma; **ι**=~113.5 Ma; **κ**=~113.3 Ma; **λ**=~113.25 Ma; **μ**=~113.0 Ma**;** **ν**=~112.3 Ma; **ξ**=~111.8 Ma and **ο**=~111.7 Ma (Figure 11). According to these ages we suggest that the following levels can be correlated with respective counterparts in the Vocontian Basin: the Jacob/113 could be related

926 with DC 2, the Monte Nerone Level with the HN2-HN7, and the Urbino Level with the HN13-
927 HN15 (Figure 11). Ba/Al and Mn/Al ratios along the PLG section show two distinct peaks in the
928 Urbino/Paquier interval (Sabatino et al., 2015). The first peak (15.6 m) represents the expression
929 of Paquier in the PLG, while the second (16.3 m) coincides with the Urbino level, highlighting
930 the presence of a pair of events associated with the landmark ξ.

931 Carbon-isotope excursions and/or organic rich-levels that define the OAE 1b have been
932 recognized in the Tethyan and North Atlantic regions (e.g., Herrle et al., 2004, 2010, 2015;
933 Trabucho-Alexandre et al., 2011; Kennedy et al., 2014; Coccioni et al., 2014). In the Vocontian
934 Basin, four organic-rich levels named Jacob, Kilian, Paquier, and Leenhardt (Bréhéret, 1994)
935 have been considered records of the OAE 1b, although some studies consider only the Jacob,
936 Kilian, and Paquier (Trabucho-Alexandre et al., 2011) or just the Paquier (Herrle et al., 2004).
937 The internal markers within the C-isotope stages recognized here can be used as reference to
938 make correlations of the OAE 1b interval worldwide.

939 The C-isotope fluctuations could result from the balance between several processes
940 recycling carbon on the Earth's surface, including the input of isotopically light volcanic $CO_2$,
941 the increased recycling rates of $^{12}C$-rich intermediate water, the intensified flux of $^{12}C$-rich
942 riverine dissolved inorganic carbon (DIC), and the thermal dissociation of methane hydrates (e.g.
943 Menegatti et al., 1998; Weissert, 1989; Bralower et al., 1999; Matsumoto et al., 2020, 2021).

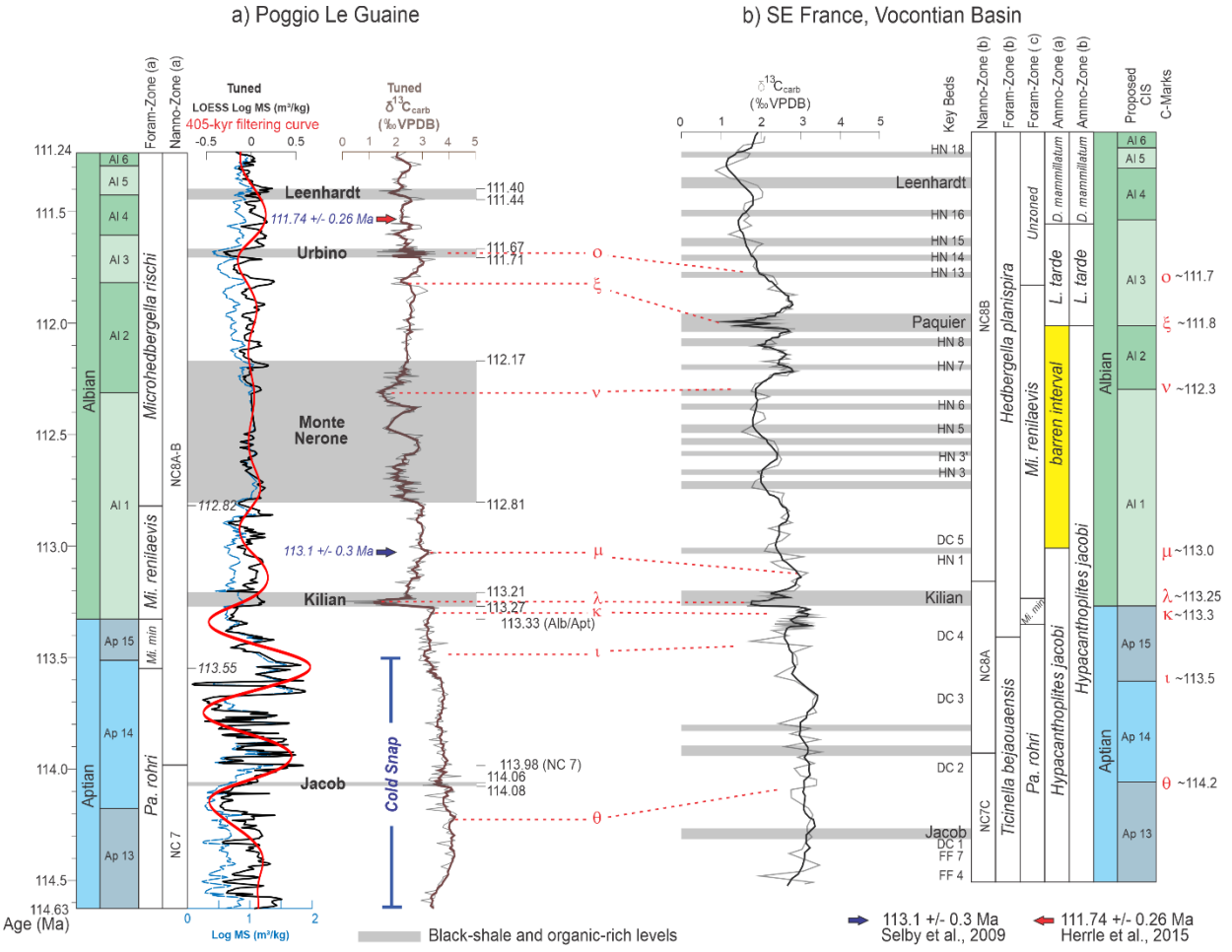


**Figure 11.** Correlation of upper Aptian-lower Albian intervals in the Umbria-Marche Basin (PLG core, on the left) with the Vocontian Basin (on the right) through $\delta^{13}C_{carb}$ records, C-isotope stages and associated markers: a) PLG foraminiferal and nannofossil zones from Coccioni et al. (2014); b) Foraminiferal and nannofossil zones from Herrle et al. (2004); b-c) Foraminiferal zone and ammonite zone from Charbonier et al. (2023) and a) Ammonite zone from Bodin et al. (2023).

The combined isotope stratigraphy of Poggio le Guaine, Vocontian Basin, DSDP Site 545, and ODP Hole 1049C records (Coccioni et al., 2014) allows us to characterize the studied interval on global scale. The new C-isotope correlation allows us to precisely calibrate the absolute age (111.74 ± 0.26 Ma for **o** marker) to be transposed into the PLG record and used as a tie-point for a new cyclostratigraphic tuning of entire studied interval. Previous studies used $^{206}Pb/^{238}U$ age of 113.1 ± 0.3 Ma determined for chemically abraded zircon from a tuff horizon 65 cm above the Aptian/Albian boundary (Selby et al., 2009) as a tie-point for the 405 kyr cycles tuning, but the tuff horizon near top *H. jacobi* ammonite zone in the Schwicheldt Ton Member,

Gault Formation (Vöhrum, Germany) was ~1000 km distant from the PLG site. Furthermore, the very top of this ammonite zone has been reported in different positions (Herrle et al., 2010; Charbonier et al., 2023; Bodin et al., 2023) and could not be correlated with a specific C-isotope stage. The top of the *H. jacobi* zone is not the best anchoring point for cyclostratigraphic studies, as it has an unconstrained age and thus cannot be correlated with the Kilian Level (Bodin et al., 2023); the Paquier level (Herrle et al., 2010) and the Leenhardt level (Charbonier et al., 2023), Figure 11b.

Bornemann et al. (2023) presented the first high-resolution CIS for the Berriasian to Coniacian interval from NW Germany that stratigraphically locates the position of the Vöhrum boundary tuff (**μ** marker) in a carbon isotope curve and proposed a slightly older age for the Aptian–Albian boundary of ca. 113.65 Ma. This estimate of the Kilian age (**λ** marker) was anchored on the cyclostratigraphic study of Nebe (1999), which provided a sedimentation rate of 3.6 cm/kyr and extended upwards 20 m of section (interval between tuff and Kilian) to conclude that the Kilian event is 555 ± 13 kyr older than the tuff. As the tuff horizon was dated at 113.1 ± 0.3 Ma (Selby et al., 2009), then the Kilian must have an age of 113.66 ± 0.3 Ma.

We conclude that transposing the **o** marker to the 111.74 ± 0.26 Ma age and test the range of possible ages of the **μ** marker is more realistic and reliable than transposing the top of the *H. jacobi* zone found in Vöhrum as marker of the Aptian-Albian boundary (Gale et al., 2020).

Even at a great distance and with the absence of bioevents common to both basins, the CIS provides: 1. the association of 111.74 ± 0.26 Ma age (**o** marker) obtained in Axel Heiberg (Herrle et al., 2015) to the OAE 1b event described on Gradstein et al. (2012), understood here as a correlation to the Urbino/Paquier at the UMB (Coccioni et al., 2012, 2014; Sabatino et al., 2015, 2018), 2, the association of tuff horizon position (**μ** marker) at the end of the **λ** excursion as 113.1 ± 0.3 Ma (Selby et al., 2009) and 3. the association of 113.66 ± 0.3 Ma for the Kilian (***k*** marker).

990

991 4.3 Paleoclimate during OAE 1b event

992 Paleoceanographic changes during the OAE 1b show that each level enriched in organic
993 matter has its own characteristics, with distinct detrital input values, different types of organic
994 matter, and varying degrees of anoxia and productivity (Erbacher et al., 1999; Sabatino et al.,
995 2015, 2018; Heimhofer et al., 2006; Matsumoto et al., 2022; Bodin et al., 2023). Likely, different
996 geological processes controlled the depositions of the black shales, resulting in a wide range of
997 variables and forcing possibilities (Table 4). However, the long lasting interval encompassing
998 this highly variable period, sometimes simplified by the concatenation and naming of various
999 distinct events by the acronym OAE 1b, leads us to attribute a volcanic origin background of
1000 Kerguelen Plateau, Broken Ridge and/or OJP (Frey et al., 2000; Whitechurch et al., 1992:
1001 Sabatino et al., 2015; Davidson et al., 2023) or a long-term orbital cycle (longer than 2 Myr) or
1002 even the effect of orbital chaotic resonance (Ma et al., 2017).

1003 Sabatino et al., (2015) concluded that the enhanced burial of barium in the latest Aptian–
1004 early Albian could reflect higher marine primary productivity, which is presumably driven by
1005 higher atmospheric $pCO_2$, enhanced terrestrial weathering and additional nutrient delivery to the
1006 ocean and, suggested that the negative excursions in the $\delta^{13}C_{carb}$ in the Kilian and Urbino/Paquier
1007 levels could be related to a major contribution of isotopically light terrestrial carbonate ions by
1008 an enhanced continental runoff during more humid conditions, as clearly testified by the detrital
1009 proxies (Sabatino et al., 2015).

1010 The PLG Aptian-Albian sediments were deposited during an exceptionally warm climate
1011 (Sabatino et al., 2015), with short term cold episodes (McAnena et al., 2013; Bottini et al., 2015;
1012 Bodin et al., 2023; Herrle et al., 2015). Some pieces of evidence support the relative short-term
1013 glacial intervals such as glendonites and deposits with affinities to glacial tillites and dropstones
1014 (Price, 1999). Our correlation based on C-isotope positions *Glendonites beds* of Axel Heilberg
1015 Island (Herrle et al., 2015) and the concurrent Cold Snap event (McAnena et al, 2013) at the
1016 PLG support the existence of cool shelf waters during late Aptian age. The basal interval of
1017 studied section of the PLG, described as Cold Snap (McAnena et al, 2013; Bottini et al., 2015;
1018 Leandro et al., 2022), is dominated by lowest levels of titanium until the planktonic foraminiferal
1019 turnover.

It is noteworthy that there is a mismatch between the peaks of Hg/TOC and levels enriched in organic matter (Sabatino et al., 2018). Also, the peaks of volcanism associated with the OAE 1b event occur only in the initial portion of the event, with a non-volcanic character being attributed to the majority of OEA 1b (Matsumoto et al., 2022), suggesting that volcanism (and the extreme climatic conditions associated with these events) are not the cause of the deposition of these levels, but rather an amplifying component of the orbital forcing that conditioned the generation of intense monsoon events and high weathering, as supported by the relationship between some enriched levels and weathering proxies. These arguments lead us to agree with the *multiple drives* mechanism proposed by Wang et al. (2022) for atmospheric-circulation reorganization.

In the PLG core series, the $CaCO_3$ curve follows a long cycle with an inverse trend respect to MS. Except from the Urbino/Paquier interval, all black shales are depleted in $CaCO_3$ reflecting fluctuations in carbonate productivity and terrigenous sediment supply. Between the Jacob Level and the planktonic foraminiferal turnover, there is an interval with high values of $CaCO_3$ and MS that could be ascribed to a deposition in a different environmental context (higher level of MS associated with high $CaCO_3$ content, a feature opposite to the entire rest of the studied interval), relative to the climax of the *Cold Snap* event (e.g., McAnena et al., 2013; Bottini et al., 2015; Leandro et al., 2022) and abnormally enriched with Mn/Al (Sabatino et al., 2015). This oscillation of ~0.5 Myr in the $CaCO_3$ data is related to an increase of MS and indicates a paleoclimatic control that changes the total amount of magnetic particles or the magnetic carrier. It is notable the presence of high orders cycles in the $CaCO_3$ data, likely associated with episodes of enhanced carbonate dissolution (Broecker and Clark, 1999).

The Ti and Fe contents are inferred here as proxies for arid and humid phases. The relationship between the phases of the signals of MS, Fe, Ti, and $CaCO_3$ suggests a common paleoclimatic control, where the orbital forcing is amplified by stochastic occurrences, corresponding to volcanic episodes and rapid atmospheric $CO_2$ input (Sabatino et al., 2015; Matsumoto et al., 2020, 2022). Heimhofer et al. (2006), on the basis of a strong increase in terrestrial palynomorphs, interpreted that the beginning of OAE 1b event in the Vocontian Basin as being primarily formed by detrital inputs from the land detrital components. Arid conditions during the late Aptian–early Albian interval with more humid condition in the uppermost Aptian

Kilian and early Albian Urbino/Paquier levels (Sabatino et al., 2015) could be a key to understand the cause (s) for organic-rich levels deposition.

Wavelengths analysis (Figures 4 and 5) suggest three different cycles, with different periods, forcing the paleoclimate: the first one, a long-period wavelength (combination of Myr cycles with 1600, 1000 and 700 kyr) with minimal values associated with Cold Snap and Monte Nerone intervals; the second wavelength that provides the alternation of carbonate bundles with black shales could be also observed in the upper section; and a third one with higher frequency, with time durations similar to those observed in the deposition of black shales. The Kilian and Leenhardt levels are positively correlated with short-term oscillations in both XRF proxies, highlighting that the increased continental sediment input, contributed to the deposition of these lithofacies. On the other hand, no relationship between increased continental input and the 113/Jacob and Urbino/Paquier levels was found. The long-term variations in Hg/TOC values associated with peaks could document that the effects of significant Hg emissions are related to the multi-phase emplacement of volcanism during the Aptian-early Albian (Sabatino et al., 2018), is probably the responsible for the termination of the arid and relatively cool conditions of the Cold Snap (McAnena et al, 2013; Wang et al., 2022).

A synthesis of studies related to the organic-enriched levels that are part of OAE 1b highlights the various mechanisms and forcings responsible for the deposition of these levels (Table 4). The variables indicate that the Jacob/113 subevent is clearly a 'volcanic' event that resulted in high productivity, as shown by volcanic indicators and the absence of weathering indicators. Pyrolysis analyses reveal that the Jacob Level is composed of continental-origin organic matter in the Vocontian Basin (Bodin et al., 2023). However, in the PLG, a significant marine contribution is present (Sabatino et al., 2015), highlighting paleogeographic control.

The Kilian subevent presents a mixed character (volcanic + monsoonal), as both the presence of continental organic matter and precursor eruptions, along with the ages of preferential plagioclases, suggest that its deposition must have been conditioned by both the induced effect of volcanic activity and the result of changes in Hadley circulation dynamics. This forced large-scale precipitation and stratification of the water column, marking the end of the Cold Snap period. In contrast to the Jacob subevent, the organic matter present in the Kilian Level is of continental origin in the PLG. However, in the Vocontian Basin (Briers section), it exhibits a substantial marine content with increased primary productivity (Bodin et al., 2023).

The cluster related to the Monte Nerone interval is very enigmatic and seems to have a mixed character. The sediments become more reddish and argillaceous, giving this interval a CORB-like characteristic (Wang et al., 2009; Coccioni et al., 2014). The high frequency of lithological intercalation, associated with sporadic inputs of terrestrial material, suggests a monsoonal character. However, the lack of correlation between volcanic indicators does not allow for a perfect characterization of this interval as volcanic.

**Table 4:** Synthesis of organic matter-rich levels paleoceanographic proxies' indicators.

| | Detrital input proxies | | Volcanism indicators | | | Productivity | | | |
|---|---|---|---|---|---|---|---|---|---|
| | Organic Matter-Type (b.) | Fe, Ti (a.) | $^{187}Os/^{188}Os$ (c.) | Hg/TOC (d.) | Plag. Ages(f.) | HI values (b.) | Aeolian input(b.) | M. palnk. archaeal (b, e.) | Ba content (a.) |
| *onset* | | | Yes? | Yes | Yes | | | | Median |
| *Jacob Level* | II (Marine contrib.) and III | Low | Yes | No | Yes | High | Yes | | Median |
| *onset* | | | Yes | Yes | Yes | | | | High |
| Kilian | III and IV (Terrestrial) | High | No | No | Yes | Low | Yes (top) | Yes | Low |
| *onset* | | | No | Yes | No | | | | High |
| M. Nerone | III and IV (Terrestrial) | es (sporadi | No | Yes (sporadic) | Yes | Low | | | Median |
| *onset* | | | No | No | Yes | | | | High |
| Urbino/Paquier | II (Marine contrib.) | No | No | No | Yes | High | | yes | High |
| *onset* | | | No | Yes | Yes | | | | Median |
| Leenhardt | III and IV (Terrestrial) | High | No | No | No | Low | | | Low |

a = This study; b = Sabatino et al., 2015; c= Matsumoto et al., 2022; d = Sabatino et al., 2018; e = Kuypers et al., 2002; f = Davidson et al., 2023

Despite the suggestion of disconnection between the Urbino and Paquier levels, at this point, given the level of detail in the studies conducted so far, we will treat them as similar intervals, as even the Paquier Level could be subdivided into two events (Erbacher et al., 1999; Kuypers et al., 2002). The clear marine contribution, evidenced by the presence of marine planktonic archaea, high productivity, extreme redox conditions (presence of redox-sensitive elements), very high thallium isotope values (Wang et al., 2022), and the absence of volcanic indicators would result in a characterization of this level as an example of a monsoonal global anoxic event. However, the lack of detrital input indicators suggests that the Paquier Level is likely associated with a major transgressive event, unlike the Leenhardt Level, which is characterized as a clearly monsoonal event (terrestrial organic matter and high values of proxies related to weathering and humidity), combined with a volcanic event, as shown by volcanic indicators, as in Table 4.

We conclude that the Cold Snap period, characterized by milder temperatures compared to the average of the Cretaceous period, comes to an end due to the input of volcanic $CO_2$ resulting from the implementation of Large Igneous Provinces (LIPs), initiating a period of

hyperthermia, heavy precipitation, intense weathering and marine primary productivity. The significant input of continental material resulting from weathering conditioned the deposition of organic-rich levels during the OAE 1b event. In chaos theory, the effect where a small change in one variable can cause significant and amplified changes in other variables is known as the "butterfly effect." Large volcanic eruptions likely played this role in paleoclimate during OAE 1b, acting as "stochastic noise" in the nonlinear paleoclimatic dynamic system. Rapid marine transgressions and atmospheric disturbances related to these peaks of volcanism served as amplifiers of orbital forcings, resulting in deoxygenation and carbon burial events deposited during OAE 1b.

## Conclusions

A cyclostratigraphic analysis was performed on the MS, Ti and Fe series of the upper Aptian-lower Albian interval from the PLG core, encompassing the pelagic Marne a Fucoidi succession of the Umbria-Marche Basin (Central Italy), which is one of the most detailed sedimentary record of this period. The new temporal calibration through the metric imposed by orbital cycles allows us to better correlate the paleoceanographic fluctuations within the OAE 1b interval with their respective forcings. On the basis of these, we provide evidence of:

1. MS, Ti and Fe data-set display a 405-kyr cycles a strong and statistically significative (> 95% CL) signal that correlates with the long-eccentricity Milankovitch cycle. Our interpretation is supported by SAR statistical tests (TimeOpt and COCO/eCOCO methodologies) resulting in an average rate of 0.5 cm/kyr. There is an evident control of SAR by weathering and terrigenous input as revealed by Ti profile.
2. By combining new biostratigraphic and high-resolution isotopic data, a 405-kyr calibrated floating astronomical timescale was constructed for the PLG core, and we can infer an age of ~113.55 for the FO of *M. miniglobularis* (6.5 m), ~113.33 Ma for the FO of *M. renilaevis* (7.7 m) and ~112.82 Ma for the FO of *M. rischi* (10.8 m).
3. Our astronomical calibration shows ~7 cycles of 405 kyr in the interval between 3.5-18 m (OAE 1b interval), which covers a timespan of ~2.68 Myr. The chronostratigraphic study also provides an age of 114.07 Ma for 113/Jacob 113.25 Ma for Kilian, 112.49 Ma as a central age of the Monte Nerone cluster, 111.69 Ma for Urbino and 111.42 Ma for

Leenhardt sub-events, and a timespan of ~20 kyr for 113/Jacob, 60 kyr for Kilian, 640 kyr for Monte Nerone cluster, 40 kyr for Urbino and 40 kyr for Leenhardt levels.

4. C-isotope stratigraphy shows an immense potential for be used as tie point for cyclostratigraphic studies and becomes a valuable way to evaluate diachronism of bioevents, allowing correlation between different basins through c-marks, with ages estimated using PLG core tuning as: **θ** = ~114.2 Ma; **ι**=~113.5 Ma; **κ**=~113.3 Ma; **λ**=~113.25 Ma; **μ**=~113.0 Ma**; ν**=~112.3 Ma; **ξ**=~111.8 Ma and **ο**=~111.7 Ma, suggesting that: Jacob/113 PLG level could be related with DC 2 of Vocontian Basin; Monte Nerone PLG level with HN2-HN7 Vocontian Basin levels and; Urbino PLG level with HN14-HN15 Vocontian Basin levels.
5. Each strata within the OAE 1b event exhibits distinct characteristics arising from the interplay of a warm climate induced by volcanic CO2 input (which acts as an amplifier of orbital forcings, driving paleoclimate changes) and oceanic-atmospheric disturbances such as heavy precipitation and intense weathering. These factors contribute to deoxygenation and carbon burial during the OAE 1b period.

## Acknowledgments

The paper is an integral part of the Project: *Processamento e interpretação de dados magnetoestratigráficos do Cretáceo das Bacias Brasileiras*, which is financially supported by Petróleo Brasileiro S.A.—Petrobras (FAURGS 8368). C.G.L. is supported by the *Conselho Nacional de Desenvolvimento Científico e Tecnológico* (CNPq – grant 141093/2018-8). J.M.F.RAMOS acknowledges Petrobras for PHD process. J.F.S also acknowledges the *Fundação de Amparo à Pesquisa do Estado do Rio Grande do Sul* (FAPERGS) (grant #16/2551-0000213-4), and CNPq (grants #304022/2018-7, #201508/2009- 5, #427280/2018-4, #311231/2021-7).

## Open Research

MS, Ti and Fe data archiving process is already underway in the ZENODO repository (DOI 10.5281/zenodo.10557295.), where the temporary upload of a copy of your data is being carried out for review purposes.

## References

Ait-Itto, F-Z., Martinez, M. , Deconinck, J. F., Bodin, S. (2023). Astronomical calibration of the OAE1b from the Col de Pré-Guittard section (Aptian-Albian), Vocontian Basin, France. *Cretaceous Research 150*. https://doi.org/10.1016/j.cretres.2023.105618

Arthur, M. A., Jenkyns, H. C., Brumsack, H. J., Schlanger, S. O. (1990). Stratigraphy, Geochemistry, and Paleoceanography of Organic Carbon-Rich Cretaceous Sequences, In book: Cretaceous Resources, Events and Rhythms (pp.75-119) Publisher: Kluwer Editors: Ginsburg, R.N. and Beaudoin, B.

Arthur, M. A., and I. Premoli Silva. (1982). Development of widespread organic carbon-rich strata in the Mediterranean Tethys, in Nature of Cretaceous Carbon-Rich Facies, edited by S. O. Schlanger and M. B. Cita, pp. 7 – 54, Academic, San Diego, Calif., 1982.

Arz, H. W., Patzold, J., & Wefer, G. (1998). Correlated millennial scale changes in surface hydrography and terrigenous sediment yield inferred from last glacial marine deposits off northeastern Brazil. *Quaternary Research, 50*(2), 157.166. doi.org/10.1006/qres.1998.1992

Bodin, S., Charpentier, M., Ullmann, C. V., Rudra, A., Sanei, H. (2023). Carbon cycle during the late Aptian–early Albian OAE 1b: A focus on the Kilian–Paquier levels interval. *Global and Planetary Change 222*: 104074

Bottini, C., Erba, E., Tiraboschi, D., Jenkyns, H. C., Schouten, S., and Sinninghe Damsté, J. S. (2015). Climate variability and ocean fertility during the Aptian Stage. *Climate of the Past, 11*(3): 383–402. https://doi.org/10.5194/cp-11-383-2015

Bottini, C. & Erba, E. (2018). Mid-Cretaceous paleoenvironmental changes in the western Tethys. *Climate of the Past, 14*: 1147–1163.

Bornemann, A., Erbacher, J., Blumenberg, M., and Voigt, S. (2023). A first high-resolution carbon isotope stratigraphy from the Boreal (NW Germany) for the Berriasian to Coniacian interval—implications for the timing of the Aptian–Albian boundary. Front. *Earth Sci. 11*:1173319. doi: 10.3389/feart.2023.1173319

Bralower, T. J., Cobabe, E., Clement, B., Sliter, W. V., Osburn, C., Longoria, J. (1999). The record of global change in mid-Cretaceous (Barremian-Albian) sections from the Sierra Madre, northeastern Mexico. *Journal of Foraminiferal Research, v. 29*, no. 4: 418–437.

Bréhéret, J-G. (1983). Sur des niveaux de black shales dans l'Albien inférieur et moyen du domaine vocontien (SE de la France): étude de nannofaciès et signification des paléoenvironnements. *Bull Mus Natl Hist Nat Paris 5*, 1, C, 1: 113–159.

Bréhéret, J-G. (1988). Episodes de sédimentation riche en matière organique dans les marnes bleues d'âge aptien et albien de la partie pélagique du bassin vocontien. *Bull Soc Géol Fr 8*, 4: 349–356.

Bréhéret, J. G. (1994). The Mid-Cretaceous Organic-Rich Sediments from the Vocontian Zone of the French Southeast Basin. In: Mascle, A. (Ed.), Hydrocarbon and petroleum geology of France. Special publication of the European Association of Petroleum Geoscientists No. 4. Springer, Berlin- Heidelberg-New York, pp. 295–320.

Broecker, W. S., Clark, E. (1999). $CaCO_3$ size distribution: A paleocarbonate ion proxy. *Paleoceanography*, 14(5), 596-604.

Browning, E. L. & Watkins, D. K. (2008). Elevated Primary Productivity of Calcareous Nannoplankton Associated with Ocean Anxoic Event 1b during the Aptian/Albian Transition (Early Cretaceous). *Papers in the Earth and Atmospheric Sciences. 237*. https://digitalcommons.unl.edu/geosciencefacpub/237

Chambers, L.M., Pringle, M.S., and Fitton, J.G. (2004). Phreatomagmatic eruptions on the Ontong Java Plateau: An Aptian 40Ar/39Ar age for volcaniclastic rocks at ODP Site 1184, in Fitton, G., Mahoney, J., Wallace, P., and Saunders, A., eds, Origin and Evolution of the Ontong Java Plateau: Geological Society, London, Special Publication 229, p. 325–331, doi:10.1144/GSL.SP.2004.229.01.18.

Charbonnier, G., Boulila, S., Spangenberg, J. E., Adatte, T., Föllmi, K. B., Laskar, J. (2023). Astrochronology of the Aptian stage and evidence for the chaotic orbital motion of Mercury. *Earth and Planetary Science Letters, 610*, 118104

1223 Channell, J.E.T., D'Argenio, B., Horvath, F. (1979). Adria, the African promontory, in Mesozoic
1224 Mediterranean paleogeography. *Earth Sci. Rev. 15*, 213–292.
1225 Coccioni, R., Nesci, O., Tramontana, M., Wezel, F.C., and Moretti, E. (1987). Descrizione di un
1226 livello–guida "radiolaritico-bituminoso-ittiolitico" alla base delle Marne a Fucoidi
1227 nell'Appennino umbro-marchigiano. *Boll. Soc. Geol. Italiana, 106*:183–192.
1228 Coccioni, R., Franchi, R., Nesci, O., Wezel, F.C., Battistini, F., and Pallecchi, P. (1989).
1229 Stratigraphy and mineralogy of the Selli Level (Early Aptian) at the base of the Marne a
1230 Fucoidi in the Umbro-Marchean Apennines, Italy. In Wiedmann, J. (Ed.), Cretaceous of
1231 the Western Tethys. Proceedings 3rd International Cretaceous Symposium, Stuttgart (E.
1232 Schweizerbart'sche Verlagsbuchhandlung), 563–584.
1233 Coccioni, R., Franchi, R., Nesci, O., Perilli, N., Wezel, F.C., and Battistini, F. (1990).
1234 Stratigrafia, micropaleontologia e mineralogía delle Marne a Fucoidi delle sezioni di
1235 Poggio le Guaine e del Fiume Bosso (Appennino umbro-marchigiano). Atti 2° Convegno
1236 Internazionale "Fossili, Evoluzione, Ambiente", Pergola, 25–30 ottobre 1987,
1237 Tecnostampa, 163–201.
1238 Coccioni, R., Erba, E., and Premoli Silva, I. (1992). Barremian-Aptian calcareous plankton
1239 biostratigraphy from the Gorgo a Cerbara section (Marche, Central Italy) and
1240 implications for plankton evolution. *Cret. Res., 13*:517–537. doi:10.1016/0195-
1241 6671(92)90015-I
1242 Coccioni, R. & Galeotti, S. (1993). Orbitally induced cycles in benthic foraminiferal
1243 morphogroups and trophic structures distribution patterns from the Late Albian
1244 "Amadeus Segment" (Central Italy). *J. Micropaleontol. 12*, 227–239.
1245 Coccioni, R., 1996. The Cretaceous of the Umbria-Marche Apennines (Central Italy). *Jost*
1246 *Wiedmann Symposium on Cretaceous Stratigraphy, Paleobiology and*
1247 *Paleobiogeography*, Tübingen, 7–10 March 1996, 129–136.
1248 Coccioni, R., 2001. The "Pialli Level" from the latest Albian of the Umbria-Marche Apennines
1249 (Italy). *Federazione Italiana di Scienze della Terra, Geoitalia 2001,* 192–193.
1250 Coccioni, R., Jovane, L., Bancalà, Bucci, C., Fauth, G., Frontalini, F., Janikian, L., Savian, J. F.,
1251 Almeida, R. P., Mathias, G. L., Trindade, R. I. F. (2012). Umbria-Marche Basin, Central
1252 Italy: A Reference Section for the Aptian-Albian Interval at Low Latitudes. *Scientific*
1253 *Drilling, No. 13,* April 2012. doi:10.2204/iodp.sd.13.07.2011

1254 Coccioni, R., Sabatino, N., Frontalini, F., Gardin, S., Sideri, M., Sprovieri, M. (2014). The
1255 neglected history of Oceanic Anoxic Event 1b: insights and new data from the Poggio le
1256 Guaine section (Umbria–Marche Basin). *Stratigraphy 11* (3–4), 245–282
1257 Cresta, S., Monechi, S., and Parisi, G. (1989). Stratigrafia del Mesozoico al Cenozoico nell'area
1258 Umbro-Marchigiana. Mem. Descr. Carta Geol. Italia, 34:185.
1259 Davidson, P. C., Koppers, A. A. P. K., Sano, T., Hanyu, T. (2023). A younger and protracted
1260 emplacement of the Ontong Java Plateau. *Science 380*: 1185–1188.
1261 Eldholm, O., Coffin, M. F. (2000). Large Igneous Province and Plate Tectonics. The Hystory
1262 and Dynamics of Global Plate Motions. *Geophysical Monograph Series 121*.
1263 Erba, E. (1988). Aptian-Albian calcareous nannofossil biostratigraphy of the Scisti a Fucoidi
1264 cored at Piobbico (central Italy). *Riv. Ital. Paleont. Strat., 94*:249–284.
1265 Erba, E. (1992). Calcareous nannofossil distribution in pelagic rhythmic sediments (Aptian-
1266 Albian Piobbico core, Central Italy). *Rivista Italiana di Paleontologia e Stratigrafia 97*,
1267 455e484.
1268 Erbacher, J., Hemleben, C., Huber, B.T., Markey, M. (1999). Correlating environmental changes
1269 during early Albian oceanic anoxic event 1B using benthic foraminiferal paleoecology.
1270 *Mar. Micropaleontol. 38*, 7–28. http://dx.doi.org/10.1016/S0377-8398(99)00036-5.
1271 Fauth, G., Krahl, G., Kochhann, K.G.D., Bom, M.H., Fauth, S.B., Bruno, M.D.R., Guerra, R. M.,
1272 Ceolin, D., Santos, A.S., Martin, J.V., Strohschoen Jr., O., Savian, J.F., Leandro, C.G.,
1273 Mello, R.G., Lima, F.H.O. (2022). Astronomical calibration of the latest Aptian to middle
1274 Albian in the South Atlantic Ocean (Sergipe-Alagoas Basin, Brazil). *Palaeogeogr.*
1275 *Palaeoclimatol. Palaeoecol. 602*, 111175. https://doi.org/10.1016/j.palaeo.2022.111175
1276 Frey, F. A., Coffin, M. F., Wallace, P. J., Weis, D., Zhao, X., Wise Jr, S. W., Wähnert, V. et al.
1277 (2000). Origin and evolution of a submarine large igneous province : the Kerguelen
1278 Plateau and Broken Ridge, southern Indian Ocean. *Earth and Planetary Science Letters*
1279 *176*, 73-89.
1280 Gale, A.S., Mutterlose, J., Batenburg, S., Gradstein, F.M., Agterberg, F.P., Ogg, J.G., Petrizzo,
1281 M.R. (2020). The Cretaceous Period. In: Geologic Time Scale 2020. Elsevier, pp. 1023–
1282 1086. https://doi.org/10.1016/B978-0-12-824360-2.00027-9.

1283 Giorgioni, M., H. Weissert, S. M. Bernasconi, P. A. Hochuli, R. Coccioni, and Keller, C. E.
1284 (2012). Orbital control on carbon cycle and oceanography in the mid-Cretaceous
1285 greenhouse, *Paleoceanography, 27*, PA1204. https://doi:10.1029/2011PA002163.
1286 Giorgioni, M., Tiraboschi, D., Erba, E., Hamann, Y., Weissert, H. (2017). Sedimentary patterns
1287 and palaeoceanography of the Albian Marne a Fucoidi Formation (Central Italy) revealed
1288 by high-resolution geochemical and nannofossil data. *Sedimentology 64 (1)*, 111-126.
1289 Gradstein, F.M., Ogg, J.G., Schmitz, M., Ogg, G. (2020). *The Geologic Time Scale 2020*.
1290 Elsevier (1390 pp.).
1291 Grippo, A., Fischer, A.G., Hinnov, L.A., Herbert, T.D., Premoli-Silva, I. (2004).
1292 Cyclostratigraphy and chronology of the Albian Stage (Piobboco Core, Italy). In:
1293 Cyclostratigraphy: approaches and case histories. Special Publication 81, 57–81.
1294 Heimhofer, U., Hochuli, P.A., Herrle, J.O., Weissert, H. (2006). Contrasting origins of Early
1295 Cretaceous black shales in the Vocontian basin: evidence from palynological and
1296 calcareous nannofossil records. *Palaeogeogr. Palaeoclimatol. Palaeoecol. 235*, 93–109.
1297 http://dx.doi.org/10.1016/j.palaeo.2005.09.025.
1298 Herbert, T. D., Fischer, A. G. (1986). Milankovitch climatic origin of mid-Cretaceous black
1299 shale rhythms in central Italy. *Nature, Vol. 321*, 19 June 1986
1300 Herrle, J. O., Kössler, P., Bollmann, J. (2010). Palaeoceanographic differences of early Late
1301 Aptian black shale events in the Vocontian Basin (SE France). *Palaeogeography,*
1302 *Palaeoclimatology, Palaeoecology 297*, 367–376.
1303 Herrle, J. O., Kössler, P., Friedrich, O., Erlenkeuser, H., and Hemleben, C. (2004). High-
1304 resolution carbon isotope records of the Aptian to Lower Albian from SE France and the
1305 Mazagan Plateau (DSDP Site 545): a stratigraphic tool for paleoceanographic and
1306 paleobiologic reconstruction. *Earth and Planetary Science Letters, 218*(1–2): 149–161.
1307 doi.org/10.1016/S0012-821X(03)00646-0
1308 Herrle, J.O., Schröder-Adams, C.J., Davis, W., Pugh, A.T., Galloway, J.M., Fath, J. (2015). Mid-
1309 cretaceous High Arctic stratigraphy, climate, and oceanic anoxic events. *Geology 43* (5),
1310 403–406. https://doi.org/10.1130/G36439.1.
1311 Huang, C., Hinnov, L. A., Fischer, A. G., Grippo, A. & Herbert, T. (2010). Astronomical tuning
1312 of the Aptian stage from Italian reference sections. *Geology 238*, 899–903 (2010).

1313 Huber, B.T., Leckie, M.R. (2011). Planktic foraminiferal species turnover across deep-sea
1314 Aptian/Albian Boundary sections. *J. Foraminiferal Res. 41*, 53–95. https://doi.org/
1315 10.2113/gsjfr.41.1.53.
1316 Jenkyns, H. C. (2010). Geochemistry of oceanic anoxic events. *Geochemistry, Geophysics,*
1317 *Geosystems, 11*(3): Q03004. doi.org/10.1029/2009GC002788
1318 Kemper, E. (1987). Das Klima der Kreide-Zeit. *Geologisches Jahrbuch Reihe A, 96*: pp. 5-185
1319 Kennedy, W.J., Gale, A.S., Huber, B.T., Petrizzo, M. R., Bown, P., Barchetta, A., Jenkyns, H.C.
1320 (2014). Integrated stratigraphy across the Aptian/Albian boundary at the Col de Pré-
1321 Guittard (southeast France): a candidate Global Boundary Stratotype Section. *Cretaceous*
1322 *Research, v. 51*, pp. 248–259.
1323 Kennedy, W.J., Gale, A.S., Huber, B.T., Petrizzo, M. R., Bown, P., Jenkyns, H.C. (2017). The
1324 Global Boundary Stratotype Section and Point (GSSP) for the base of the Albian Stage,
1325 of the Cretaceous, the Col de Pré-Guittard section, Arnayon, Drôme, France. *Episodes*
1326 *Vol. 40, No. 3*, pp. 177–188.
1327 http://dx.doi.org/10.18814/epiiugs/2017/v40i3/017021Kochhann, M. V. L., Cagliari, J.,
1328 Kochhann, K. G. D., & Franco, D. R. (2020). Orbital and millennial scale cycles paced
1329 climate variability during the Late Paleozoic Ice Age in the southwestern Gondwana.
1330 *Geochemistry, Geophysics, Geosystems, 21*, e2019GC008676.
1331 https://doi.org/10.1029/2019GC008676
1332 Kuypers, M. M. M., Blokker, P., Hopmans, E. C., Kinkel, H., Pancost, R. D., Schouten, S.,
1333 Sinninghe Damsté, J. S. (2002). Archaeal remains dominate marine organic matter from
1334 the early Albian oceanic anoxic event 1b. *Palaeogeogr. Palaeoclimatol. Palaeoecol. 185*,
1335 211–234. http://dx.doi.org/10.1016/S0031-0182(02)00301-2.
1336 Larson, R. L., & Erba, E. (1999). Onset of the mid-Cretaceous greenhouse in the Barremian-
1337 Aptian: Igneous events and the biological, sedimentary, and geochemical responses,
1338 *Paleoceanography, 14*, 663 – 678.
1339 Laskar, J., Robutel, P., Joutel, F., Gastineau, M., Correia, A.C.M., Levrard, B., (2004). A long-
1340 term numerical solution for the insolation quantities of the Earth. *Astron. Astrophys. 428*,
1341 261–285. https://doi.org/10.1051/0004-6361:20041335.

1342 Laskar, J., Fienga, A., Gastineau, M., and Manche, H. (2011a). La2010: a new orbital solution
1343 for the long-term motion of the Earth. *Astronomy & Astrophysics, 532*.
1344 doi:10.1051/0004-6361/201116836.
1345 Laskar, J., Fienga, A.; Gastineau, M., and Manche, H. (2011b). La2010: a new orbital solution
1346 for the long-term motion of the Earth. *Astronomy & Astrophysics, 532*: A89.
1347 doi:10.1051/0004-6361/201116836.
1348 Laskar, J., Gastineau, M., Delisle, J., Farrées, A., and Fienga, A. (2011c). Strong chaos induced
1349 by close encounters with ceres and vesta. *Astronomy and Astrophysics, 532*: L4.
1350 Laskar, J. (2020). Astrochronology. In book: Geologic Time Scale 2020, pp. 139-158.
1351 Leandro, C.G., Savian, J.F., Kochhann, M.V.L., Franco, D.R., Coccioni, R., Frontalini, F.,
1352 Gardin, S., Jovane, F., Figueiredo, M., Tedeschi, L.R., Janikian, L., Almeida, R.P.,
1353 Trindade, R.I.F. (2022). Astronomical tuning of the Aptian stage and its implications for
1354 age recalibrations and paleoclimatic events. *Nat. Commun.13*, 2941. https://doi .org /10
1355 .1038 /s41467-022-30075-3.
1356 Leckie, R. M., Bralower, T. J., Cashman, R. (2002). Oceanic anoxic events and plankton
1357 evolution: Biotic response to tectonic forcing during the mid-Cretaceous.
1358 *Paleoceanography*, *17*(3): 13-11–13-29. https://doi.org/10.1029/2001PA000623
1359 Li, M., Hinnov, L., Kump, L. (2019). Acycle: Time-series analysis software for paleoclimate
1360 research and education. *Comput. Geosci. 127*, 12–22.
1361 https://doi.org/10.1016/j.cageo.2019.02.011.
1362 Li, M., Kump, L., Hinnov, L., Mann, M. E. (2018). Tracking variable sedimentation rates and
1363 astronomical forcing in Phanerozoic paleoclimate proxy series with evolutionary
1364 correlation coefficients and hypothesis testing. *Earth and Planetary Science Letters 501*,
1365 165–179. https://doi.org/10.1016/j.epsl.2018.08.041
1366 Liu W., Wu H., Hinnov L.A., Xi D., He H., Zhang S., Yang T. (2020). Early Cretaceous
1367 Terrestrial Milankovitch Cycles in the Luanping Basin, North China and Time
1368 Constraints on Early Stage Jehol Biota Evolution. *Front. Earth Sci. 8*:178. doi:
1369 10.3389/feart.2020.00178
1370 Ludvigson, G.A., Joeckel, R.M., Gonzalez, L.A., Gulbranson, E.L., Rasbury, E.T., Hunt, G. J.,
1371 Kirkland, J.I., Madsen, S. (2010). Correlation of Aptian-Albian Carbon Isotope

Excursions in Continental Strata of the Cretaceous Foreland Basin, Eastern Utah, U.S.A. *J. Sediment. Res. 80*, 955–974. https://doi.org/10.2110/jsr.2010.086

Ma, C., Meyers, S. R., Sageman, B. B. (2017). Theory of chaotic orbital variations confirmed by Cretaceous geological evidence. *Nature 542* (7642), 468–470.

Mann, M. E., Lees, J. M. (1996). Robust Estimation of Background Noise and Signal Detection in Climatic Time Series. *Climatic Change*, Vol. 33, pp. 409-445.

Matsumoto, H., Kuroda, J., Coccioni, R., Frontalini, F., Sakai, S., Ogawa, N.O., Ohkouchi, N., (2020). Marine Os isotopic evidence for multiple volcanic episodes during Cretaceous Oceanic Anoxic Event 1b. *Sci. Rep. 10* (1), 12601. https://doi.org/10.1038/s41598-020-69505-x.

Matsumoto, H., Coccioni, R., Frontalini, F., Shirai, K., Jovane, L., Trindade, R. I. F., Savian, J. F., Tejada, M. L. G., Galdin, S., Kuroda, J. (2021). Long-term Aptian marine osmium isotopic record of Ontong Java Nui activity: *Geology, v. 49*, p. 1148–1152, https://doi.org/10.1130/G48863.1

Matsumoto, H., Coccioni, R., Frontalini, F., Shirai, K., Jovane, L., Trindade, R., Savian, J. F., Kuroda, J. (2022). Mid-cretaceous marine Os isotope evidence for heterogeneous cause of oceanic anoxic events. *Nat. Commun. 13 (1)*, 239. https://doi.org/10.1038/s41467-021-27817-0.

McAnena, A., Flögel, S., Hofmann, P., Herrle, J.O., Griesand, A., Pross, J., Talbot, H.M., Rethemeyer, J., Wallmann, K., Wagner, T. (2013). Atlantic cooling associated with a marine biotic crisis during the mid-cretaceous period. *Nat. Geosci. 6* (7), 558–561. https://doi.org/10.1038/ngeo1850.

Menegatti, A. P., Weissert, H., Brown, R. S., Tyson, R. V., Farrimond, P., Strasser, A., and Caron, M. (1998). High-resolution $\delta^{13}C$ stratigraphy through the Early Aptian "Livello selli" of the Alpine tethys. *Paleoceanography*, *13*(5): 530–545. https://doi.org/10.1029/98PA01793

Meyers, S. R., B. Sageman, and Hinnov, L. (2001). Integrated quantitative stratigraphy of the Cenomanian-Turonian Bridge Creek Limestone Member using evolutive harmonic analysis and stratigraphic modeling, *J. Sediment. Res.*, *71*, 627–643.

1401 Meyers, S. R. (2015). The evaluation of eccentricity-related amplitude modulation and bundling
1402 in paleoclimate data: An inverse approach for astrochronologic testing and time scale
1403 optimization. *Paleoceanography, 30*, 1625–1640. https://doi.org/10.1002/2015PA002850
1404 Meyers, S. R. (2019). Cyclostratigraphy and the problem of astrochronologic testing. *Earth Sci.*
1405 *Rev. 190*, 190–223. https://doi: 10.1016/j.earscirev.2018.11.015
1406 Nebe, D. W. (1999). Zyklenuntersuchungen an unterkretazischen Sedimenten in NW-
1407 Deutschland - Nachweisbarkeit von Milankovitch-Zyklen. Phd thesis. Ruhr-Univ.
1408 Bochum.
1409 Ogg, J. G. & Hinnov, L. (2012). In: *The Geologic Time Scale 2012* (eds Grandstein, F.M. et al.).
1410 793–853. Elsevier, 2012.
1411 Ogg, J.G., Ogg, G. and Gradstein, F. M. (2016). *A Concise Geologic Time Scale: 2016*.
1412 Amsterdam: Elsevier, p. 234.
1413 Petrizzo, M.R., Huber, B.T., Gale, A.S., Barchetta, A., Jenkyns, H.C. (2012). Abrupt planktic
1414 foraminiferal turnover across the Niveau Kilian at Col de Pré-Guittard (Vocontian Basin,
1415 Southeast France): new criteria for defining the Aptian/Albian boundary. *Newsl. Stratigr.*
1416 *45* (1), 55.
1417 Pokorný, J., Suza, P., Pokorný, P., Chlupáčová, M., and Hrouda, F. (2006). Widening power of
1418 low-fi eld magnetic methods in the investigation of rocks and environmental materials
1419 using the Multi-Function Kappabridge Set: *Geophysical Research Abstracts, v. 8*, abs.
1420 EGU 06-A-04141.
1421 Price, G. D., and Gröcke, D. R. (2002). Strontium-isotope stratigraphy and oxygen and carbon-
1422 isotope variation during the Middle Jurassic–Early Cretaceous of the Falkland Plateau,
1423 South Atlantic. *Palaeogeography, Palaeoclimatology, Palaeoecology, 183*(3–4): 209–
1424 222. https://doi.org/10.1016/S0031-0182(01)00486-2
1425 Savian, J. F., Trindade, R. I. F., Janikian, L., Jovane, L., Almeida, R. P., Coccioni, R., Frontalini,
1426 F., Sideri, M., Figueiredo, M. F. (2016). The Barremian-Aptian boundary in the Poggio le
1427 Guaine core (central Italy): evidence for magnetic polarity Chron M0r and oceanic
1428 anoxic event 1a. *Geol. Soc. Am. Spec. Pap. 524*, 57–78.
1429 Sabatino, N., Coccioni, R., Manta, D. S., Baudin, F., Vallefuoco, M., Traina, A., Sprovieri, M.
1430 (2015). High-resolution chemostratigraphy of the late Aptian–early Albian oceanic
1431 anoxic event (OAE 1b) from the Poggio le Guaine section (Umbria–Marche Basin,

central Italy). *Palaeogeography, Palaeoclimatology, Palaeoecology 426*, 319–333. dx.doi.org/10.1016/j.palaeo.2015.03.009

Sabatino, N., Ferraro, S., Coccioni, R., Bonsignore, M. Del Core, M., Tancredi, V., Sprovieri, M. (2018). Mercury anomalies in upper Aptian-lower Albian sediments from the Tethys Realm. *Palaeogeography, Palaeoclimatology, Palaeoecology 495*, 163–170. doi.org/10.1016/j.palaeo.2018.01.008

Satolli, S., Besse, J., and Calamita, F. (2008). Paleomagnetism of Aptian–Albian sections from the Northern Apennines (Italy): Implications for the 150–100 Ma apparent polar wander of Adria and Africa: *Earth and Planetary Science Letters, v. 276*, p. 115–128, doi:10.1016/j.epsl.2008.09.013.

Schlanger, S. O., and Jenkyns, H. C. (1976). Cretaceous oceanic anoxic events: causes and consequences. *Geologie en Mijnbouw, 55*: 179–184.

Selby, D., Mutterlose, J. & Condon, D. J. (2009). U-Pb and Re-Os Geochronology of the Aptian/Albian and Cenomanian/Turonian stage boundaries: implications for timescale calibration, osmium isotope seawater composition and Re-Os systematics in organic-rich sediments. *Chem. Geol. 265*, 394–409. https://doi.org/10.1016/j.chemgeo.2009.05.005.

Schulz, M., and Stattegger, K. (1997). Spectrum: Spectral analysis of unevenly spaced paleoclimatic time series. *Computers & Geosciences 23*, No. 9, pp. 929-945

Tateo, F., Morandi, N., Nicolai, A., Ripepe, M., Coccioni, R., Galeotti, S., Baudin, F. (2000). Orbital control on pelagic clay sedimentology: the case of late Albian "Amadeus Segment" (central Italy). *Bull. Soc. Géol. France, t. 171*, n° 2: 217-228

Tedeschi, L. R., Jenkyns, H. C., Robinson, S. A., Sanjinés, A. E. S., Viviers, M. C., Quintaes, C. M. S. P., and Vazquez, J. C. (2017). New age constraints on Aptian evaporites and carbonates from the South Atlantic: Implications for Oceanic Anoxic Event 1a. *Geology, v. 45*; no. 6; p. 543–546. doi:10.1130/G38886.1

Tejada, M. L. G. et al. (2009). Ontong Java Plateau eruption as a trigger for the early Aptian oceanic anoxic event. *Geology 37*, 855–858.

Thomson, D.J. (1982). Spectrum estimation and harmonic analysis. Proc. IEEE 70,1055–1096.

Tiraboschi, D., Erba, E., and Jenkyns, H.C. (2009). Origin of rhythmic Albian black shales (Piobbico core, central Italy): Calcareous nannofossil quantitative and statistical analyses

and paleoceanographic reconstructions: *Paleoceanography, v. 24,* PA2222, doi:10.1029/2008PA001670.

Tornaghi, M.E., Premoli Silva, I., and Ripepe, M. (1989). Lithostratigraphy and planktonic foraminiferal biostratigraphy of the Aptian-Albian "Scisti a Fucoidi" in the Piobbico core, Marche, Italy: Background for cyclostratigraphy: *Rivista Italiana di Paleontologia e Stratigrafi a, v. 95*, p. 223–264.

Trabucho Alexandre, J., Van Gilst, R. I., Rodríguez-López, J. P., and De Boer, P. L. (2011). The sedimentary expression of oceanic anoxic event 1b in the North Atlantic. *Sedimentology, 58*(5): 1217–1246. doi.org/10.1111/j.1365-3091.2010.01202.x

Turchyn, A.V., Schrag, D.P., Coccioni, R., and Montanari, A. (2009). Stable isotope analysis of the Cretaceous sulfur cycle. *Earth Planet. Sci. Lett., 285*:115–123.

Waltham, D. (2015). Milankovitch Period Uncertainties and Their Impact On Cyclostratigraphy. *Journal of Sedimentary Research; 85* (8): 990–998. https://doi.org/10.2110/jsr.2015.66

Wang, C., Hu, X., Huang, Y., Scott, R. W., Wagreich, M. (2009). Overview of Cretaceous Oceanic Red Beds (CORBs): a window on global oceanic and climate change. S. S. 91, Cretaceous Oceanic Red Beds: Stratigraphy, Composition, Origins, and Paleoceanographic and Paleoclimatic Significance: pp. 13-33.

Wang, Y., Bodin, S., Blusztajn, J. S., Ullmann, C., Nielsen, S. G. (2022). Orbitally paced global oceanic deoxygenation decoupled from volcanic CO2 emission during the middle Cretaceous Oceanic Anoxic Event 1b (Aptian-Albian transition). *Geology, v. 50,* n° 11. 259 (Cambridge University Press, 2003). p. 1324–1328, https://doi.org/10.1130/G50553.1

Weedon, G. P. (2003). *Time Series Analysis And Cyclostratigraphy: Examining Stratigraphic Records of Environmental Cycles*, Vol. 259 (Cambridge University Press, 2003).

Weissert, H. (1989). C-isotope stratigraphy, a monitor of paleoenvironmental change: a case study from the Early Cretaceous, *Surv. Geophys.*, in press, 1989.

Whitechurch, H., Montigny, R., Sevigny, J., Storey, M., Salters, V.J.M. (1992). K–Ar and $^{40}Ar/^{39}Ar$ ages of central Kerguelen Plateau basalts. *Ocean Drill. Program Sci. Results 120*, 71–77.

1491 Zhang, Y., et al. (2021). Magnetostratigraphy of U-Pb–dated boreholes in Svalbard, Norway,
1492 implies that magnetochron M0r (a proposed Barremian-Aptian boundary marker) begins
1493 at 121.2 ± 0.4 Ma: *Geology*, *v. 49*, p. 733–737, https://doi.org/10.1130/G48591.1
1494